PAPER • OPEN ACCESS

Validation of SART 3.5D algorithm for cerebrovascular dynamics and artery versus vein classification in presurgical 3D digital subtraction angiographies

To cite this article: Sara El Hadji *et al* 2022 *Phys. Med. Biol.* **67** 185018

IOP Publishing Phys. Med. Biol. 67 (2022) 185018 https://doi.org/10.1088/1361-6560/ac8c7f

Physics in Medicine & Biology

IPEM Institute of Physics and Engineering in Medicine

OPEN ACCESS

RECEIVED
5 April 2022

REVISED
25 July 2022

ACCEPTED FOR PUBLICATION
24 August 2022

PUBLISHED
16 September 2022

PAPER

Validation of SART 3.5D algorithm for cerebrovascular dynamics and artery versus vein classification in presurgical 3D digital subtraction angiographies

Sara El Hadji[1,*], Augusto Bonilauri[1], Elena De Momi[1], Laura Castana[2], Antonio Macera[3], Luca Berta[4], Francesco Cardinale[2,5] and Giuseppe Baselli[1]

[1] Department of Electronics, Information and Bioengineering, Politecnico di Milano, Milan, Italy
[2] Claudio Munari Center for Epilepsy Surgery, ASST Grande Ospedale Metropolitano Niguarda, Milan, Italy
[3] Department of Neuroradiology, ASST Grande Ospedale Metropolitano Niguarda, Milan, Italy
[4] Department of Medical Physics, ASST Grande Ospedale Metropolitano Niguarda, Milan, Italy
[5] Department of Medicine and Surgery, Unit of Neuroscience, Universita' degli Studi di Parma, Parma, Italy
[*] Author to whom any correspondence should be addressed.

E-mail: sara.elhadji@polimi.it

Keywords: computed tomography, time resolved angiography, iterative reconstruction technique, O-arm, artery vein classification

Abstract

Classification of arteries and veins in cerebral angiograms can increase the safety of neurosurgical procedures, such as StereoElectroEncephaloGraphy, and aid the diagnosis of vascular pathologies, as arterovenous malformations. We propose a new method for vessel classification using the contrast medium dynamics in rotational digital subtraction angiography (DSA). After 3D DSA and angiogram segmentation, contrast enhanced projections are processed to suppress soft tissue and bone structures attenuation effect and further enhance the CM flow. For each voxel labelled as vessel, a time intensity curve (TIC) is obtained as a linear combination of temporal basis functions whose weights are addressed by simultaneous algebraic reconstruction technique (SART 3.5D), expanded to include dynamics. Each TIC is classified by comparing the areas under the curve in the arterial and venous phases. Clustering is applied to optimize the classification thresholds. On a dataset of 60 patients, a median value of sensitivity (90%), specificity (91%), and accuracy (92%) were obtained with respect to annotated arterial and venous voxels up to branching order 4–5. Qualitative results are also presented about CM arrival time mapping and its distribution in arteries and veins respectively. In conclusion, this study shows a valuable impact, at no protocol extra-cost or invasiveness, concerning surgical planning related to the enhancement of arteries as major organs at risk. Also, it opens a new scope on the pathophysiology of cerebrovascular dynamics and its anatomical relationships.

1. Introduction

Cerebrovascular tree visualization plays a crucial role in neuroimaging and neurosurgery in preoperative, intraoperative, and postoperative phases (Serafin *et al* 2012, Ilunga-Mbuyamba *et al* 2016, Teng *et al* 2016, Ramakonar *et al* 2018, Neumann *et al* 2019, Perin *et al* 2021). Beyond a purely morphological angiography, the separation of arteries and veins (A/V) can be extremely advantageous in several clinical procedures, with a major impact on surgical planning and navigation (Kruger *et al* 2018, Tomasi *et al* 2020). For example, in keyhole neurosurgery procedures such as StereoElectroEncephaloGraphy (SEEG), hemorrhage is one of the most commonly occurring complication, which makes recognition and safeguarding of arteries a major requirement (Nowell *et al* 2015, Gilard *et al* 2016, Gonzalez-Martınez *et al* 2016, Mullin *et al* 2016, Minkin *et al* 2017, Sparks *et al* 2017, Neumann *et al* 2019, Vakharia *et al* 2018, 2019, Scorza *et al* 2021). Additionally, in procedures such as arteriovenous malformations (AVMs) embolization, clinicians would benefit from the selective visualization of the feeding arteries and the venous drainage network to guarantee major safety and efficacy of the surgical

resection (Kaminogo *et al* 2002, Chen *et al* 2017, Prada *et al* 2018). Moreover, the observation of the venous system can help the detection of vascular abnormalities such as arteriovenous shunts (Gandhi *et al* 2012, Gomez *et al* 2012).

The gold standard technique procedure for visual assessment of the cerebrovascular tree morphology is the digital subtraction angiography (DSA) (Mistretta 1980). The DSA is the result of a subtraction between an image acquired before the administration of contrast medium (CM) from the one acquired after contrast agent propagation in the bloodstream. Consequently, in the DSA dataset, projections are acquired at different time intervals resulting in a collection of frames describing the flow of the CM through the vessels over a scan time which covers the CM transport to the whole cerebrovascular tree (Christenson *et al* 1980). This information apart from being used for cerebrovascular morphology assessment represents an optimal surrogate marker for cerebral hemodynamics.

Previous attempts to reconstruct image-based cerebral hemodynamics flow patterns exploited 2D catheter cerebral DSA images and tackled CM extraction by recording the intensity values along the projection frames for each individual pixel (Strother *et al* 2010, Gölitz *et al* 2013, Scalzo and Liebeskind 2016, Teng *et al* 2016, Hong *et al* 2019). To reduce random noise the curves are generally fitted with prior distributions from which perfusion parameters are computed analytically (Lin and Jackson 2012). Once extracted, the perfusion parameters are parametrized to generate color-coded DSA images and perfusion maps. However, despite the high temporal and spatial resolution (Christenson *et al* 1980), this technique still suffers from confounding factors due to superimpositions of blood vessels located at different depths and vascular foreshortening. (Scalzo and Liebeskind 2016, Teng *et al* 2016, Hong *et al* 2019).

These flaws were partially addressed with the development of rotational three-dimensional (3D) DSA suites equipped with flat panel detector computed tomography (CT) (Green *et al* 2004, Akpek *et al* 2005). Similar to the use of more conventional angiographic equipment, 3D DSA is the result of subtracting an image without CM (bone-mask, BM) from the contrast enhanced (CE) one. A few available systems exploit software-driven subtraction of bony topography in serial rotational planes to estimate 3D vascular anatomy, guaranteeing superior spatial resolution compared to images obtained by means of CT or magnetic resonance (MR) angiography (MRA). However, if on one hand, the introduction of 3D-DSA addresses the problem of vessel overlapping, on the other hand it lacks the temporal resolution of biplanar DSA.

In this perspective, several authors reported methods that aim to reconstruct a time-resolved 3D cone beam CT (CBCT) angiography to enable the view of the anatomy not only in any desired view but also at any desired phase of vascular filling. As such, Mistretta (2011), Davis *et al* (2013), Chen and Li (2015, 2017), Sandoval-Garcia *et al* (2016), Li *et al* (2018), Ruedinger *et al* (2021) propose to employ low-angle numerical reconstructions to furnish a series of angiograms at subsequent times. At this purpose, C-arm rotational acquisition is used to acquire images before and during bolus injection. To reduce low-angle reconstruction artifacts, while providing sufficient time resolution, protocols are based on repeated scans with fast back-and-forth to capture the full cycle of the bolus inflow and washout through the vasculature.

Besides the diagnosis and treatment of vascular pathologies (Torné *et al* 2019), even stereotactic procedures demonstrated to benefit from the use of 3D-DSA. This is especially the case of SEEG, an invasive procedure in which about 10–20 intracerebral electrodes are percutaneously implanted in the brain region. This procedure requires brain vessels to be carefully avoided during the advancements of the recording electrodes into the intracranial space, with a particular caution towards arteries. Cardinale *et al* (2013, 2015) have first proposed the use of a mobile O-ring cone-beam CT (CBCT) scanner to obtain a set of datasets to be post-processed with a dedicated workflow aimed at generating 3D CBCT DSA (Cardinale *et al* 2013, 2015, 2017, 2019). The acquisition protocol proposed in Cardinale *et al* (2013, 2015) enables to capture a consistent number of projections along a full rotation which allows to accurately record the wash in phase, enhancing both the arterial and the venous tree. However, in the current processing pipeline, time-dependent information is lost, and the final 3D DSA reconstruction protocol is only able to depict a temporally averaged image of the vascular dynamic enhancement, without any distinction between arteries and veins.

In this specific context, most of the studies found in literature addressing exclusively A/V classification are based on 4D CT acquisition protocol. This technique consists in a dynamic acquisition protocol based on multiple gantry rotations which capture a sequence of 3D volumes over time, associating to each vascular voxel a Time Intensity Curves (TIC) describing the CM dynamic. Needless to say that these high-end multi-detector row CT scanners are based on highly demanding equipment and protocols requiring higher acquisition time which increases the dosage of CM and radiation exposure (Matsumoto *et al* 2005, Mendrik *et al* 2010, Laue *et al* 2013, Havla *et al* 2015, Shirasaka *et al* 2017, Meijs and Manniesing 2018, 2019).

In this work we propose a method for: (i) time-resolving the 3D DSA, (ii) providing a more advanced interpretation of the intracranial vascular tree, i.e. A/V separation, exploiting the 3D CBCT angiography imaging protocol proposed in Cardinale *et al* (2013). The main objective of this study is the recovery of the lost dynamic (hence, functional) information along the 3D DSA reconstruction pipeline and its integration within

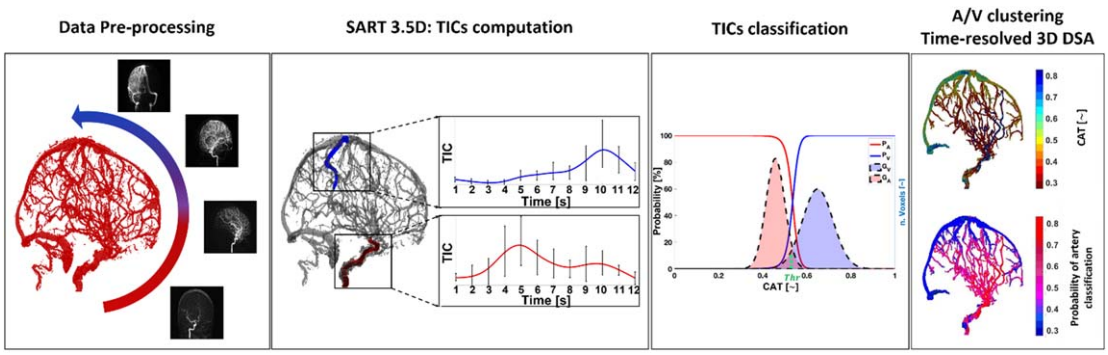

Figure 1. The proposed methodology follows four main steps (black blocks) to time resolve 3D angiography and label arteries (A) and veins (V) starting from the raw dataset. The pre-processing block (section 2.1) includes the brain vascular segmentation (par. 2.1.1) and the background subtraction in the raw data (par. 2.1.2). Then, 4D reconstructions are computed using SART 3.5D algorithm which output time intensity curves (TICs) (section 2.2) which are processed according to an area under the curve based criteria as described in section 2.3 through which the contrast time-of-arrival map and brain A/V classification are computed.

the anatomical angiographic reconstruction, starting from the standard BM and CE acquisition, with no Rx dose or CM added. This strategy was named 3.5D as it reconstructs 4D information (volume plus time) from standard 3D scans. The approach of this study is theoretically presented by Barra *et al* (2016) and is limited to a proof of concept on a low-dimension digital phantom (50^3 voxels) and a simple geometry, composed of a few vessels (~5).

The present work aims at extending the previous theoretical phantom study to clinical data. The final physiological and clinical goals were: (i) verify algorithm convergence on clinical dataset dimensions ($192 \times 512 \times 512$ voxels), real % of the targeted angiographic voxels, and real CM infusion dynamics; (ii) assess the algorithm capability to provide time resolved 3D angiographies to the finest arterial and venous branching orders, (iii) enhance and validate the previously proposed automatic artery/vein (A/V) classification in the presence of the time overlaps displayed by physiological data.

Here, results are presented relevant to 60 standard DSA datasets and validated by the accuracy of A/V classification versus a specifically developed semiautomatic annotation. These datasets provide a benchmark to evaluate the feasibility of this approach in presence of healthy and physiological blood flow circulation and vascular morphology. Further analyses addressed the comparison between the proposed TICs modelling and other TIC parameters found in literature. Qualitative results are also presented about CM arrival time mapping and its distribution in arteries and veins respectively. To our knowledge, this is the first study which validates on clinical data the proposed strategy for time resolved rotational angiography and A/V classification.

2. Materials and methods

As summarized by figure 1, the proposed method starts after the 3D DSA acquisition workflow described in section 3.1 (Cardinale *et al* 2015) by two pre-processing steps (figure 1 left panel; see section 2.1): (i) the segmentation of vessels in the angiographic volume; (ii) subtraction of BM re-projections (synthetized from the registered BM volume) from the raw CE projections. Next the TICs are computed for all the segmented vascular voxels by SART 3.5D (figure 1, 2nd panel; see section 2.3). The algorithm starts from the usual algebraic description of 3D reconstruction solved by simultaneous algebraic reconstruction technique (SART). Each voxel intensity value is substituted by a weighted linear combination of time basis functions. As such, a new algebraic problem is derived where the new unknowns are the basis function weights. The increase in unknowns is largely compensated by the sparse reconstruction which addresses only vascular voxels and solved by SART iterations. Next (figure 1, 3rd panel; see section 2.4) a contrast arrival time (CAT) parameter is extracted from each TIC and the overall distribution analyzed by a Gaussian mixture model (GMM) to determine the subject-specific separation point for A/V classification (figure 1, 4th panel, top). In addition, CAT maps are provided (bottom), which furnishes further information beyond the A/V classification.

2.1. Data pre-processing

As sketched in figure 2, data pre-processing includes: (i) the standard DSA, consisting in the reconstruction and of BM and CE volumes, their rigid registration, and subtraction; (ii) angiographic segmentation (see Par.2.1.1); and (iii) the 2D subtraction from CE projection data of the re-projections of the co-registered BM volume (see Par.2.1.2). The applied 3D reconstruction algorithm was SART, in keeping with the further steps applying the

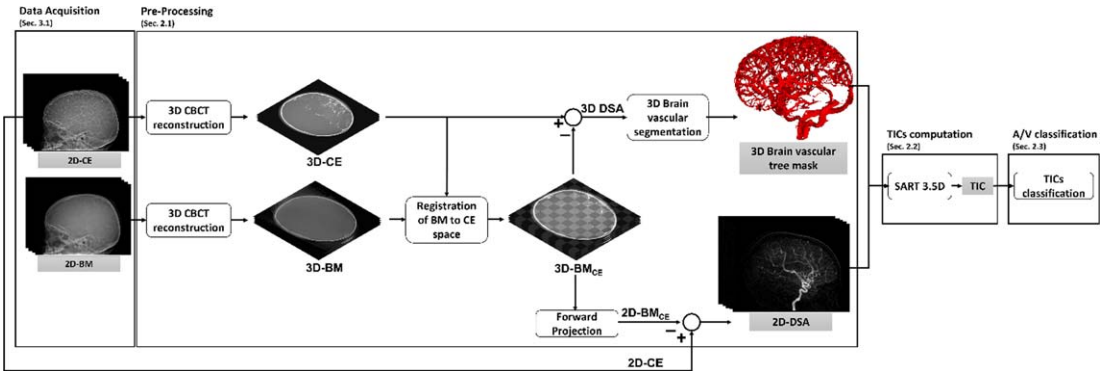

Figure 2. The proposed methodology follows three main steps (black blocks) to label arteries (A) and veins (V) starting from the raw dataset, namely, identified as contrast-enhanced (2D-CE) and bone-mask (2D-BM) as described in section 3.1. The pre-processing block (section 2.1) can be divided into two subparts. Firstly, projections data are reconstructed: the volumes, 3D-CE and 3D-BM, are then aligned by means of rigid registration. The obtained 3D- BM_{CE} is used twice. First, it is subtracted from 3D-CE to compute the 3D DSA for the brain vascular mask (par 2.1.1.). Second, it is forward projected and subtracted from the 2D-CE to obtain the 2D bone-free CE raw projection data (par. 2.1.2). Then, 4D reconstructions are computed using SART 3.5D algorithm which outputs time intensity curves (TICs) (sec) and classified.

dynamic SART modification, i.e. SART 3.5D. The standard SART was implemented with non-negativity constraint and fixed iteration number $= 5$. BM to CE registration was implemented by FLIRT of FSL (Jenkinson and Smith 2001).

Some important technical notes are anticipated here since they involve the overall quality of the pre-processing steps. Firstly, SART displayed high sensitivity to non-even processing, even if the iterative updates were weighted by the angular sample size, which resulted in hyperintensity of the overrepresented angles. The relevant artifacts were unobservable in the BM and CE reconstructed volumes. Conversely, they had remarkable effects over the BM re-projections and, hence, on the cleaned CE projections to be input to SART 3.5D. The problem was fully solved by the even resampling at 1°.

Secondly, specific attention was devoted to the construction of the system matrix $\boldsymbol{A}$, which contains the weights a_{ij} representing the intersection of the ith CB ray with the jth voxel. Comparisons showed that the distance-driven approach (De Man and Basu 2004) outperformed the voxel-driven (Siddon 1985) and the ray-driven (Joseph 1982) approaches, concerning the smoothness of reconstructed volumes. Importantly, the same system matrix A was used for: (i) SART reconstructions, (ii) registered BM re-projections, (iii) SART 3.5D, although with proper masking of non-vascular voxels.

Finally, consistent computational and memory saving was obtained by computing $\boldsymbol{A}$ for angle $\theta = 0°$ only. Projections at a generic angle θ were implemented by counter-rotanting the volume by $-\theta$, performing the projection, and rotating the volume back by θ. Rotations were implemented by a bi-linear interpolation in the rotated volume slices.

2.1.1. 3D cerebrovascular segmentation

The angiographic segmentation is common practice, in the clinical analysis of DSA. In this case, it becomes a must as *a priori* input to SART 3.5D, defining the voxel set targeted for dynamic reconstruction. The DSA underwent classical vessel enhancement filtering (Frangi *et al* 1998) and then were thresholded through an interactive tool for medical imaging segmentation, ITKsnap (Yushkevich *et al* 2006). The thresholded angiogram was refined by morphological operations and connected component analysis (CCA). Dilation and bridging (Kong and Rosenfeld 1996) were carried out to connect broken vessels. Next, CCA eliminated wrongly segmented voxels related to BM residuals and streak artifacts. Thresholding was tuned considering the minimum connected component size, the latter assessed by the 26-voxel neighborhood.

2.1.2. 2D bone-mask subtraction from CE projections

Significant coordinate changes take place between the two scans, mainly due to the catheterization and infusion preparation occurring in-between, which may require repositioning of the patient's head and of the O-arm scanner. Clearly, BM to CE co-registration cannot be computed in the 2D projection space, given the 3D rototranslation to be corrected. Conversely, the already co-registered volume 3D-BM_{CE} provides synthetic projections in the CE space, by re-projecting it through the system matrix $\boldsymbol{A}$. As said, $\boldsymbol{A}$ was computed for $\theta = 0°$ only, so, projections at $\theta \neq 0°$ were obtained by counterrotating 3D-BM_{CE}.

As sketched in the block diagram of figure 2, the cleaning of 2D-CE (i.e. the raw CE projections) by 2D-BM_{CE} produces a synthetized 2D-DSA dataset, which is next input to SART 3.5D. As shown in figure 3, the CM

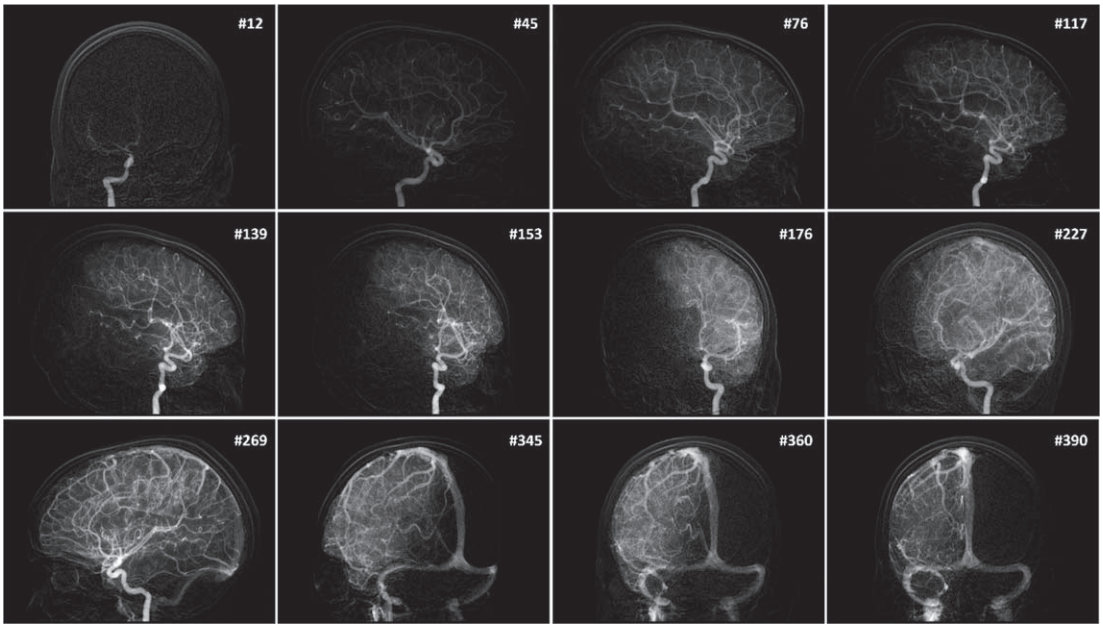

Figure 3. Representative frames from contrast-enhanced bone-free raw data obtained from subtraction between the CE raw data and the projected 3D registered bone-mask; three phases namely, the arterial, capillary, and venous phases can be distinguished while the CM is flowing through the cerebrovascular tree. The frame number is shown in each case.

Table 1. List of symbols used in section 2.

Parameter	Value
$\boldsymbol{p}$	Projection data
$\boldsymbol{\mu}$	Voxel intensities
$\boldsymbol{A}$	System matrix
I	Number of FPDs detectors
J	Number of voxels
n	Iteration number
λ	Relaxation factor
θ	View angle
Θ	Total Angular span
B	Number of basis function
$q(t)$	Basis function
$d_{(j,b)}$	Dynamic weight
K	Unknows of SART 3.5D

dynamics (from ICA, to arteries, to veins, to large veins and sinuses) is more clearly visible in the cleaned 2D-DSA. Importantly, view angles had also a precise time labeling $t = (\theta/360^{\circ}) \bullet 12$ s, with frame time resolution $\Delta t = 0.033$ s.

2.2. SART 3.5D for TICs computation

The TICs reconstruction problem is formulated as a dynamic imaging model problem which is solved by means of a sparse and time variant extended iterative reconstruction technique. Among the iterative reconstruction algorithms in literature, we opted for SART for its updating strategy which allowed us to exploit the relationship between angle θ and time t crucial for the purpose of this study. SART applies the correctional error term by grouping into a subset all projection rays from a single view angle θ, $\{p_i\}_\theta$ with index $i \in \{i\}_\theta$ (Andersen and Kak 1984). For further details on the static SART please refer to the appendix. Table 1 reports symbols used in this section.

The basic passages from static SART to the dynamic SART 3.5D are here summarized. The SART update equation is reported below:

$$\mu_j^{(n+1)} = \mu_j^{(n)} + \lambda \frac{1}{\sum_{i \in I_\theta} a_{ij}} \sum_{i \in I_\theta} \frac{p_i - \bar{p}_i^n}{\sum_{j=1}^{J} a_{ij}} a_{ij}, \tag{1}$$

updates $\boldsymbol{\mu}^{(n)} \rightarrow \boldsymbol{\mu}^{(n+1)}$ (i.e. from update n to update $n+1$ of the current estimate of $\boldsymbol{\mu}$) and is based on the simulated projection:

$$\bar{p}_i^n = \sum_{j=1}^{J} a_{ij} \mu_j^{(n)}. \tag{2}$$

In SART 3.5D the μ_j is substituted by the TIC $\mu_j(t)$ which describes the CM dynamics in the jth voxel. $\mu_j(t)$ is modelled as a linear combination of regularly shifted basis functions $q_b(t)$:

$$\mu_j(t) = \sum_{b=1}^{B} d_{j,b} \quad q_b(t), \tag{3}$$

where $d_{j,b}$ denotes the b basis function weight associated to the jth voxel. The weighting factors $[d_{j,1},\ldots,d_{j,b},\ldots, \quad d_{j,B}]$ represent the new unknowns.

B is the number of basis functions, which, after comparison of several numbers (see results) was set to 12, which, greatly limited the number of unknowns, compared to 360 time samples, still permitting to fit the regular CM dynamics. Importantly, this 12-fold increase of unknowns compared to the static problem is by far compensated by targeting the angiographic volume fraction (AVF), which is in the order of 1%. Hence, the final number of unknowns is $K = J \bullet B \bullet \text{AVF} < J < I$ is minor than the number of data J, which is a precondition to convergence. The new vector of unknowns is $\boldsymbol{d} = (d_{k(j,b)}) \in \mathbb{R}^K$. Accordingly, the dynamic algebraic equations, modelling CE projection cleaned by BM_{CE}, are:

$$\bar{p}_i = \sum_{j=1}^{J} a_{ij} \sum_{b=1}^{B} d_{j,b} \quad q_b(t). \tag{4}$$

The coefficients of the dynamic system matrix $\boldsymbol{A_B}(t)$ are given by:

$$a_{ik(j,b)}(t) = a_{ij} q_b(t), \tag{5}$$

where time t, determining the correct phase of each basis function, is obtained from the view angle with $t = 12(\theta/360°)$ s. To summarize, the proposed dynamic imaging system is defined as:

$$\boldsymbol{A_B}(\boldsymbol{t})\boldsymbol{d} = \boldsymbol{p}, \tag{6}$$

with $\boldsymbol{A_B}(\boldsymbol{t}) = (a_{ik(j,b)}(t)) \in R^{IxK}$. Its construction implies the following steps:

(i) Targeting—delete unknowns with index j out of the angiographic segmentation mask and the related system matrix columns.

(ii) Dynamics—expand the vector of unknowns by substituting to each angiographic μ_j with B basis function weights $d_{j,b}$ and the respective system matrix columns by the $a_{ik(j,b)}(t)$ of (6).

As to the SART 3.5D update was accordingly modified:

$$d_{k(j,b)}^{(n+1)} = d_{k(j,b)}^{(n)} + \lambda \frac{1}{\sum_{i \in \{i\}_\theta} a_{ik(j,b)}(\theta)} \sum_{i \in I_\theta} \frac{p_i - \bar{p}_i^{(n)}}{\sum_{j=1}^{J} a_{ik(j,b)}(\theta)} a_{ik(j,b)}(\theta). \tag{7}$$

Once the vector of jth voxel weight coefficients are computed, the TIC is finally obtained as the weighted sum of the basis functions.

Practically, the implemented algorithm, avoided the reordering work of the theoretical formulation (6). More simply, separate volumes were created for each basis function weight $d_{j,b}$, which were rotated, updated, and counter-rotated.

In summary, in the proposed SART 3.5D algorithm, the 2D-DSA input is synthetized by 2D subtraction from the raw 2D-CE projection of the 2D-BM_{CE} reprojections (after 3D coregistration to the CE space). So, SART 3.5D address only the contrast induced by the CM and, in the updates of equation (7), targeting (i.e. masking of the system matrix by the segmented angiogram) affects both the simulated projections $\bar{p}_i^{(n)}$ and the back-projection of error $p_i - \bar{p}_i^{(n)}$. Accordingly, initialization is set to zero. It is worth recalling that the dynamics represented by TICs is estimated considering a separate volume for each dynamic basis function.

The order in which the projections are accessed in the iterative reconstruction algorithms has a strong influence on the convergence speed, the accuracy, and artifacts (Guan and Gordon 1996). In SART 3.5D the applied accessing order is the multilevel access ordering scheme (MLS) in which two sequential views are chosen

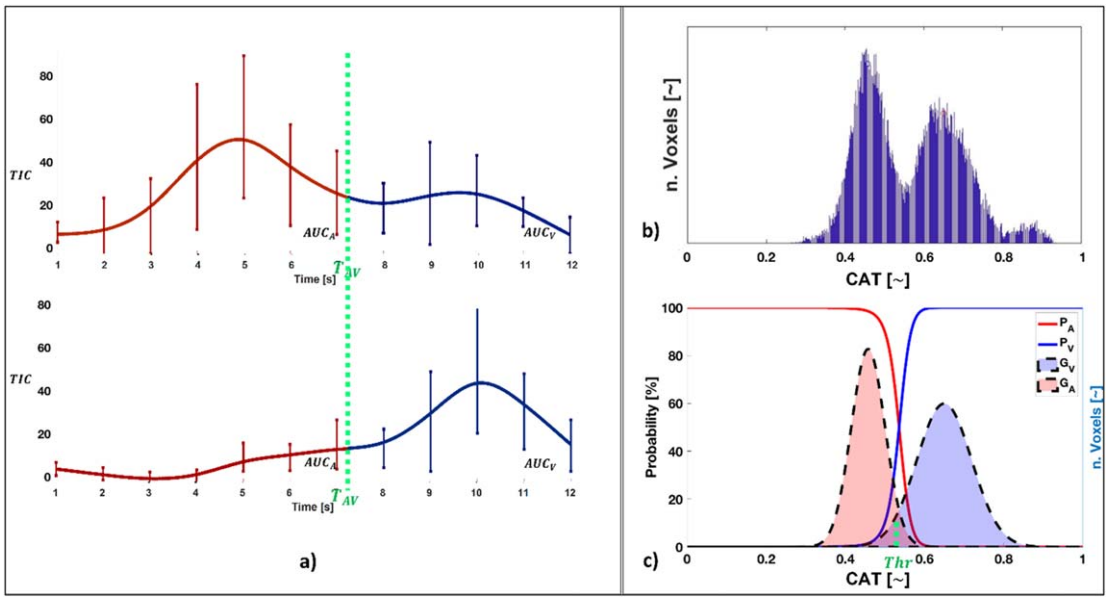

Figure 4. Overview of the TIC's classification step: (a) exemplative set of TICs selected from two separate ROIs are examined. Statistics of arterial (top) and venous (bottom) TICs with $T = 12$ s are represented. In each plot, two areas under the curve (AUC) with respect to an optimal $T_{A/V}$ are highlighted, AUC_a and AUC_v respectively; (b) and (c) from top to down: the $CAT \approx \frac{AUC_V}{AUC}$ histogram of the subset (b) is clustered by two Gaussian mixture models, G_A and G_V respectively (c). Finally the $T_{A/V}$ was computed as the temporal instant that maximizes the bimodality of the corresponding $CAT \approx \frac{AUC_V}{AUC}$ histograms. Accordingly, the probability inversion value defined as *thr* is the analytical intersection point between the identified Gaussian modes and the respective posterior probabilities (P_A and P_V). Patient case scenario (m/37 y).

for maximum orthogonality between them such that they contain a maximum of independent information in terms of angular viewing positions (Guan and Gordon 1994).

2.3. TICs classification

Most of the works addressing A/V classification require for each voxel a time-intensity profile from which signal features are extracted and then processed for classification. Laue *et al* (2013) and Meijs and Manniesing (2018, 2019) processed 4D CT scans and used unsupervised K-means clustering and a 3D convolutional neural network on time intensity signal for A/V classification, respectively. Matsumoto *et al* (2005) and Shirasaka *et al* (2017), defined the optimal scan timing for A/V separation in 4D CT as the peak-to-peak time between measured time-attenuation curves observed in manually selected ROIs. Mendrik *et al* (2010) proposed a method based on computed tomography perfusion (CTP) scans and classified the time intensity profiles according to their time to peak (TTP). While Havla *et al* (2015) extract the maximum enhancement (ME), the TTP and the full curve width half maximum (FWHM). These parameters are processed by means of a statistical method which aims at finding their optimal linear combination able to distinguish between the arterial and venous phase.

In this study, given the infusion protocol, the reconstructed TICs are characterized by a smooth step-up shape which mainly captures the wash-in phase of the CM flow. The raising phase is expected to be early in arteries and late in veins (figure 4(a)). Accordingly, we use a classification criterion that requires a separation time $T_{A/V}$ between a prevalently arterial phase and the next venous phase. The temporal segmentation permits to compare the area under the curve (AUC) in the venous phase $[T_{A/V};T]$, called AUC_V to the total AUC, which index provides the A/V classification rule:

$$\begin{cases} if \quad \frac{AUC_V}{AUC} < thr \rightarrow artery \\ if \quad \frac{AUC_V}{AUC} > thr \rightarrow vein \end{cases}, \tag{8}$$

where threshold $0 < thr < 1$ is determined to optimize the classification.

A subject-specific data-driven tuning of $T_{A/V}$ and *thr* was needed to consider the variability in the subjects' hemodynamics and CM infusion. This was carried out by unsupervised GMM clustering (Par. 2.4.2) (Dempster *et al* 1977).

Moreover, for a more intuitive understanding we convert the abovementioned classification parameter as follows:

$$CAT = \frac{AUC_V}{AUC} T, \tag{9}$$

where CAT represents a temporally scaled perfusion parameter. The working hypothesis here maintained is that the integral ratio $\frac{AUC_V}{AUC}$ is nearly proportional to the transport delay to the addressed voxel. The CAT, therefore, is only an estimate of the time of arrival of the CM, which should consider the almost sigmoidal TIC expected with perfusion protocols. In the noisy environment of real TICs, such integral estimator is considered more robust than others based on TIC morphology.

In our preliminary analyses the CAT index showed a continuum if small vessels were included. This was attributed to partial temporal superposition of the arterial and venous phases in small vessels. So, it was decided to perform a temporal based A/V classification only on 60% of voxels within vessels of larger radius, which limitation still permits to pinpoint arteries and arterioles of interest as surgical organs at risk. Hence the A/V classification was preceded by a dimension-based segmentation in Par. 2.4.1.

2.3.1. Skeletonization and radius estimation of vascular limbs

The selection of angiographic voxels undergoing A/V classification was based on the skeletonization of both the arterial and the venous tree, which implied the *a priori* exclusion of the few small vessels artifactually non-connected to the overall angiogram. Skeletonization was carried out by parallel medial axis thinning in 3D (Lee *et al* 1994). Branching points were defined as skeleton voxel with more than two neighbors (Kong and Rosenfeld 1996) and segmented the skeleton limbs. The average radius of the lth limb, $r^{(l)}$ was approximately measured considering the curvilinear cylinder cross-section area $\pi (r^{(l)})^2$ as ratio of the limb volume in number of voxels, $N^{(l)}$, divided by the skeleton length along its $n^{(l)}$ elements:

$$r^{(l)} = \sqrt{\frac{N^{(l)}}{\pi \sum_{m=1}^{n^{(l)}-1} \sqrt{(x_{m+1}^{(l)} - x_m^{(l)})^2 + (y_{m+1}^{(l)} - y_m^{(l)})^2 + (z_{m+1}^{(l)} - z_m^{(l)})^2}}}, \tag{10}$$

where x, y and z are the skeleton limb coordinates, which Euclidean distances are summed to provide the limb axis length.

2.3.2. Artery and vein clustering optimization

The angiographic limbs were ordered by descending $r^{(l)}$ and a reduced A/V clustering set was built including limbs from largest to smaller up to the inclusion of at least the 60% of all angiographic voxels. So, the about 40% of the angiogram that included arterioles and venules with large dynamic overlap was excluded from the A/V classification. The CAT index was computed on the splined TICs resampled at 0.01 s (see figure 4(a)).

As shown in figure 4(b), the CAT index of the 60% reduced set presented the expected A/V bimodal separation in all subjects, which permitted GMM clustering (Dempster *et al* 1977) and the subject-specific calibration of T_{AV} and Thr parameters.

The stochastic parallel search, a genetic algorithm (Goldberg 1989), was used to find the optimal $T_{A/V}$ within the [4-9] s time window, leading to the best GMM separation. Among various objective functions (e.g. Akaike's (Akaike 1974), Bayesian (Schwarz 1978), Kullback–Leibler information criteria (Kullback 1997), and Bhattacharya distance (Bhattacharyya 1943) the Bhattacharya (Bh) distance was chosen, which quantifies the closeness between the GMM components in terms of their overlap area. The stopping rule was set at a tolerance of 10–4.

The GMM model offers a probabilistic classification which needs conversion to a crispy rule fixing the Thr value. On preliminary trials, the most common separation criterion at equal probability density value (figure 4(c)) outperformed the alternative of balancing the probabilities of the overlapped tails. This simple criterion was consequently adopted.

2.4. Time-resolved 3D digital subtraction angiography

The CAT dynamic information was accordingly represented in false colors of the 3D angiogram, thus proposing a 4D DSA. The 'hsv' colormap with linear color scaling over the whole [0; T] range was kept as first explorative plot. This representation reflects the temporal progress of the CM in the vascular tree. Heat ('hot' in Matlab) maps with intensity based scale (arteries hotter) provide an effective representation of the contrast agent flow rate. This representation provides a more intuitive visual description of the contrast injection protocol. In particular it reflects the continuous inflow of the agent along all the acquisition window. Future applications should permit to set both the central time (most likely with the individual $T_{A/V}$ as default) and the CAT range with changing color, to enhance color contrast in the desired angiographic section. Finally, interactively scrolling through limited ranges of CAT, should provide an effective 4D representation.

Table 2. O-ARM^{TM} geometry and acquisition parameters.

Parameter	Value
Volume dimension	512 × 512 × 192
Voxel spacing	0.415 mm
Slice thickness	0.833 mm
FPD dimension	1024 × 384
Pixel size	0.776 × 0.388 mm
Source to isocenter	647.7 mm
Detector to isocenter	520.7 mm
Number of projections	390
Range rotational angle	Full rotation
Acquisition time	12 s

3. Experimental protocol

3.1. Study population, equipment, and acquisition protocol

Data from 60 consecutive subjects (31 males and 29 females, age 32 ± 13 years) who had undergone CBCT DSA for SEEG planning between 2017 and 2021 were retrospectively selected and processed. Only one internal carotid artery (ICA) CM dataset was processed for each subject, and other optional CM datasets (contralateral ICA or vertebral artery) were ignored. Therefore, 120 datasets (60 BM, 60 ICA CM) were used. All patients were suffering from partial epilepsy and did not present any vascular pathology. The technique originally developed and implemented at 'Claudio Munari' center for performing 3D CBCT DSA in the context of epilepsy surgery has been detailed elsewhere (Cardinale *et al* 2013, 2015). Briefly, the workflow includes the acquisition of a BM dataset followed by a variable number of enhanced datasets obtained during the trans-femoral selective injection of CM in at least one ICA and, when needed, in the contralateral ICA and/or in one of the vertebral arteries. The CM datasets are acquired over 12 s after the start of iopamidol (300 mg ml^{-1}) infusion in the selected artery. The injection parameters are: acceleration and deceleration 0.5 s; pressure limit 500 psi; velocity, 1.5 ml s^{-1} or 2 ml s^{-1} for children less than 25 kg and remaining patients, respectively; injection length, 10 s.

CBCT scans were obtained by means of O−arm system (Medtronic; Minneapolis, Minnesota, USA) a mobile radiographic device for intraoperative imaging originally developed for spine surgery. The device is composed by an x-ray tube (120 kWP, x-ray tube current 32–40 mA) and a flat panel detector (384 × 1024 detectors, with 0.776 × 0.388 mm detector pixel size) that rotates inside a circular gantry around the iso-center. The number of full scan projections acquired is 390, covering a total angular span of 360°. The angular sampling at regime velocity is 1° of arch; however, it is denser in the starting acceleration phase and in the deceleration phase. Irregular sampling was corrected by even interpolation and resampling at 1°. The reconstructed image consists of a 192-slice volume, 512 × 512 matrix each slice, with 0.415 × 0.415 × 0.833 mm anisotropic voxel size (volumetric field of view of 22 × 22 × 17 cm^3). All acquisition and geometric parameters are reported in table 2. Conventionally, we will refer to 'raw/projection data' as the result of a standard natural logarithmic transformation of the recorded x-ray attenuation.

3.2. Ground truth annotation

The proposed A/V classification was validated against a semi-automatic A/V annotation based on two limited angle 3D reconstructions centered on the arterial and the venous phase, respectively. The rationale was assuming that specific low-angle sets contained the main information relevant to the arterial and venous phases. 2D-DSA projections (i.e. CE projections, cleaned from BM_{CE} reprojections) were visually inspected to select two time-frames most representative of either phase. This selection was performed manually, and it is patient specific. Each limited angle set included a minimum of 30° centered on the reference frame but was widened to include as many frames representative or the arterial or the venous phase as possible. A SART limited angle volume reconstruction followed. Given the CM infusion protocol, the 'venous phase' volume enhanced both arteries and veins. Accordingly, the arterial volume was subtracted from the venous one to keep only the venous contrast, as shown in figure 5 (block diagram in the bottom panel). Hard thresholding provided a first coarse angiographic mask, next refined by local adaptive thresholding. Two expert graders manually checked and further refined the labeled ground-truth exploiting both temporal maximum intensity projection (MIP) and views from anatomical planes. A 3D medical imaging visualization tool, ITKsnap (Yushkevich *et al* 2006), was used at this purpose. Finally, morphological opening and connectivity analysis were applied to remove thin non-connected vessels and to isolate major structures. The example in figure 5, shows the annotated arterial and venous ROIs. Visual inspection confirmed the limited-angle 'gold-standard' reached branching orders up to

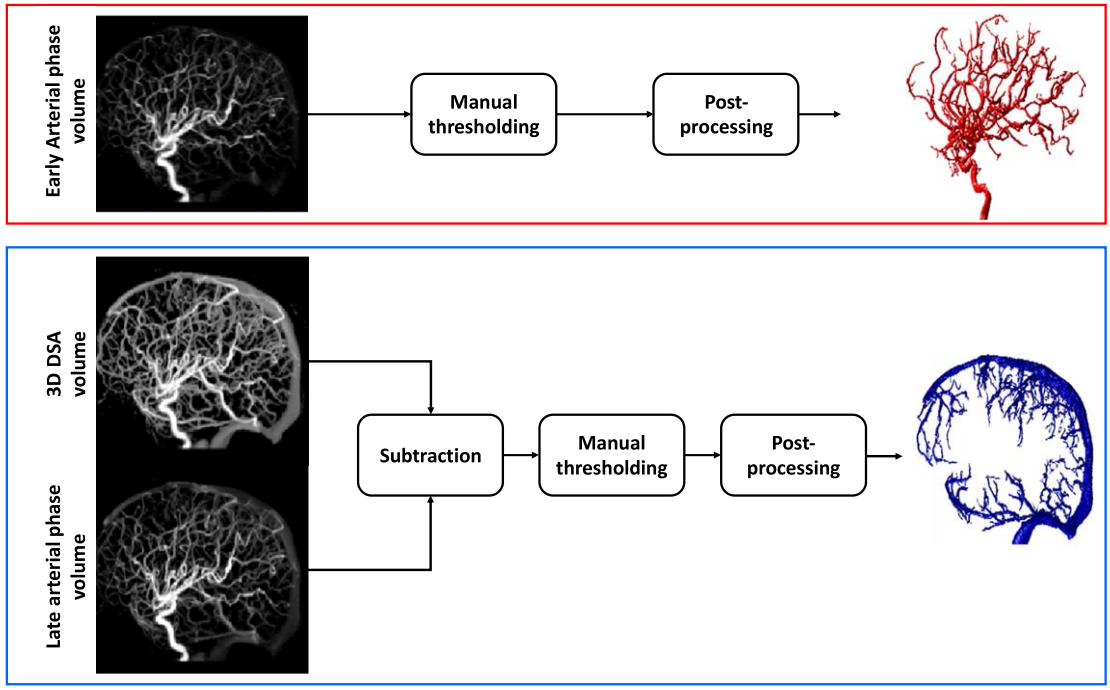

Figure 5. On the top panel: limited angle reconstruction given a set of projections including exclusively the arterial phase. In the bottom panel the limited angle reconstruction of a volume generous towards the arterial phase and fully in the initially capillary phase is reconstructed. Then is subtracted from the 3D DSA volume to preserve the venous phase of the enhancement. The two volumes are manually thresholded, and morphological operators are applied to isolate the maximum connected object.

4–5th, and despite more limited than the 60%, including clinically relevant arteries and veins on several axial slices throughout the scan, and thus it was sufficiently rich for our validation to furnish a representative ground truth, which would have been hardly achieved by a fully manual annotation which could not go beyond few vessels within the 2nd–3rd branching order. In the annotated ROIs we recognized the ICA and vessels belonging to the Anterior Cerebral artery and the Middle Cerebral Artery, while the venous ROIs included the superior, transverse, and sigmoid sinuses and major frontal, middle, parietal, temporal superficial veins terminating in the sinuses.

3.3. Comparative methods

3.3.1. SART 3.5D test-variant on raw CE data

The test-variant here described addresses iterations on the whole CE dataset, without prior BM subtraction, to be conversely performed at the very end. Main steps are as follows: (i) initialization to 3D-BM_{CE}; (ii) untargeted projection simulations $\bar{p}_{i,CE}{}^{(n)}$; (iii) errors $p_{i,CE} - \bar{p}_{i,CE}{}^{(n)}$ by comparison with the raw CE projections; (iv) targeted backprojection of errors (i.e. only the angiographic voxels are updated); (v) final subtraction of the 3D-BM from the reconstructed volumes relevant to each temporal basis function and consequent TIC extraction.

Note that now the focus on CM induced changes is within the iterations, subtracting the prior image data given by the 3D-BM_{CE}. We adapted to our case some of the theoretical steps introduced in Chen *et al* (2008). It can be easily shown that the considered errors are the same as in (7), since the BM projections can be subtracted from $p_{i,CE}$, which fits the definition of the 2D-DSA, i.e. p_i. Similarly, the same subtraction can be done on the $\bar{p}_{i,CE}{}^{(n)}$, which focuses changes from the starting BM initialization. So, in principle, the same objective function is maintained, i.e. nulling errors versus the CM additional contrast by updating exclusively the angiographic voxels. This test-variant was analyzed since similar strategies are in the literature Li *et al* (2018). Focus was on the convergence capability, which was expected to be hindered by small errors derived as difference between the large full CE and BM contrasts. Qualitative results will be shown in section 4.1, limited to the basic choice of non-overlapped, rectangular basis functions.

3.3.2. SART 3.5D test-variant with updates on progressive angles

This second test-variant was analyzed mainly to verify the convergence degradation compared to the optimal max-orthogonality subset ordering criterion. Moreover, by imposing non-overlapped, rectangular basis functions, the algorithm mimics limited-angle dynamic reconstructions, with angular range $360°/B = 30°$, with $B = 12$. Accordingly, the time resolution of TICs 1 sample/s.

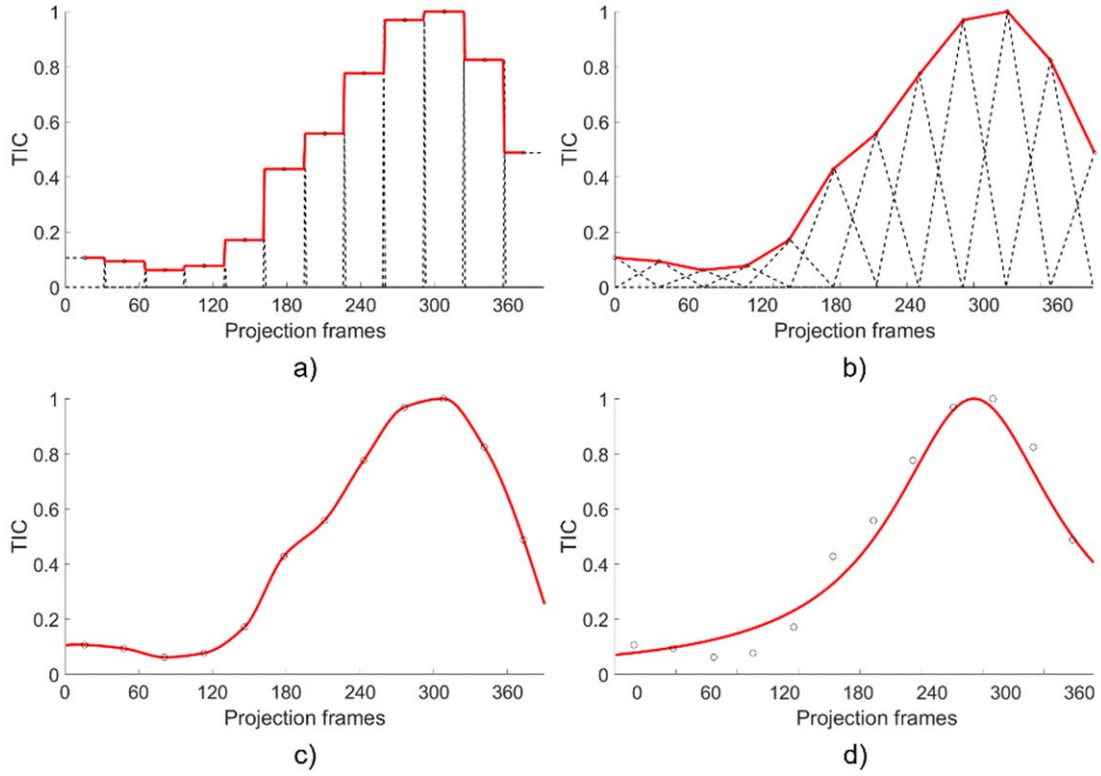

Figure 6. (a) step-wise raw TIC after rectangular basis functions; (b) linear wise raw TIC after triangular basis functions; (c) cubic spline of the step-wise TIC in panel a; (d) gamma curve fitting of the step-wise TIC in panel a.

3.3.3. Basis functions and TIC post-processing

In a previous work Barra *et al* (2016), rectangular non-overlapped basis functions are tested yet stressing the algorithm flexibility in the choice of different basis functions. As shown in figure 6, this study tested both rectangular non-overlapped basis functions (panel a) considered 50% overlapped triangular basis function to perform linear interpolation, promoting smoothness over orthogonalization. As it regards the optimal number of basis functions we examined the number of basis functions, by comparing B values ranging from 10 to 60 basis functions. Both the step-wise and the linear-wise TICs were smoothed by cubic hermite spline interpolation (see figure 6(c) for the smoothed step-wise TIC; the smoothed linear-wise is not shown).

Smoothing by parametric fitting was also considered. Curves suggested in literature as models of CM dynamics are the gamma-curve (Thompson *et al* 1964, Lin and Jackson 2012), shown in figure 6(d). The fitting was performed assuming the TIC following a two-parameter Weibull curve. The fitting was performed using the non-linear least-squares optimization method (Kenney and Keeping 1962).

3.4. Comparative perfusion parameters from TICs

From previous paragraph, the following quantitative perfusion parameters are extracted from TIC fitted with gamma-curve: the peak value, the raise time, TTP and the respective maximum value at the TTP (ME), wash in (WI) and wash out (WO) rate (computed as the time needed to raise the intensity from the baseline value to half maximum and from the peak value to half maximum, respectively) and the FWHM (Thompson *et al* 1964).

3.5. Performance metrics and statistical analysis

The performance of SART 3.5D method is evaluated by comparing the classification results to ground truth. Since arteries are the main organs at risk in surgery, their correct classifications were conventionally taken as true positives, while the correct classifications of veins were considered true negatives. Accordingly, arteries misclassified as veins were false negatives and veins misclassified as arteries were false positives. With this convention, The A/V sensitivity (Se) and specificity (Sp) reflect the model capability for correctly detecting arteries and veins, respectively. While the accuracy (Acc), quantifies the overall performance of the algorithm. The metrics have been computed individually for each case, and the median (IQR) of all score values obtained is reported as summary statistics.

To check normality, the Kolmogorov–Smirnov test was applied to all data. Comparison between groups of several independent samples was performed using the Wilcoxon Signed-Rank Test when normality could not be

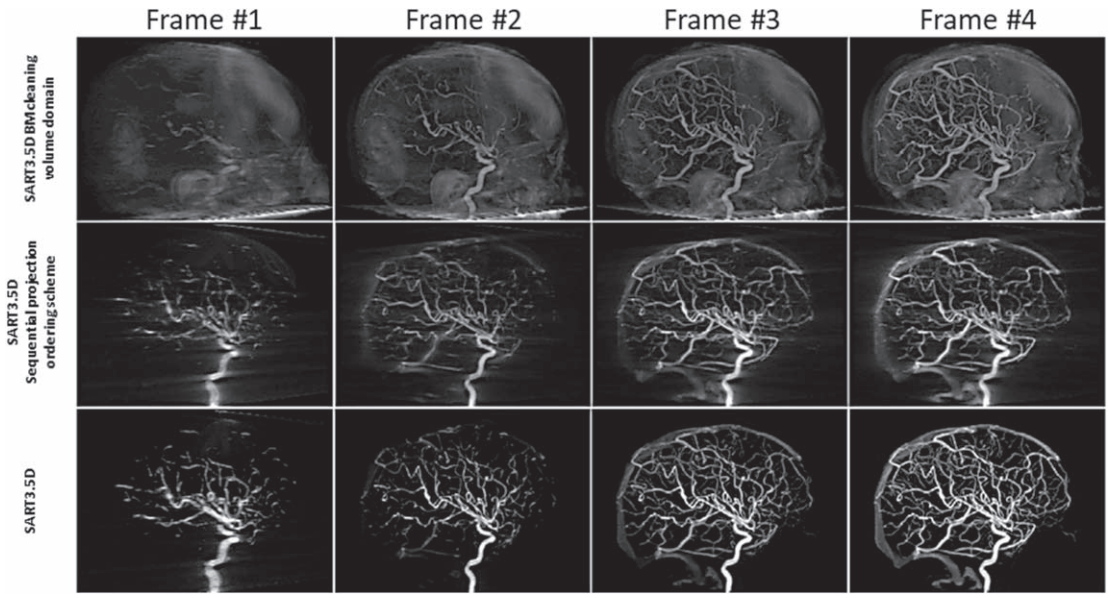

Figure 7. MIP of temporal 3D DSA in 4 different time frames. On the first row the dynamic SART 3.5D output with the BM cleaning at the end of the reconstruction. On the middle row, the dynamic SART 3.5D output with the BM cleaning performed *a priori* in the projection domain processing the projection sequentially as in a limited angle reconstruction. The bottom row instead the output of SART 3.5D obtained by preprocessing projections according to the MLS scheme.

assumed. The p values to be considered as significant is <0.05. We corrected for the effect of multiple comparisons by conducting *a posteriori* Bonferroni test by the Bonferroni factor. All statistical analysis was conducted using version 17.0 of SPSS for Windows (SPSS, Chicago, IL).

4. Results

We conducted a systematic evaluation of the algorithm modules and parameters. In this section we expose the findings of the experiments carried out to evaluate their impact on the overall performance. Results will be presented both in quantitative and qualitative terms.

4.1. SART 3.5D: pre-processing and projection ordering scheme

In this section we show different versions of SART 3.5D to evaluate the contribution of some crucial steps presented in the proposed TICs computation workflow. Specifically, SART 3.5D workflow was degraded to observe the effect of two important factors. First, we addressed the effectiveness of the BM cleaning which is carried out *a priori* in the projection domain: the same algorithm is modified to execute the BM subtraction on the fly in the volume domain. Second, we assessed SART 3.5D applied considering a projection ordering scheme that promotes orthogonalization versus a sequential projection ordering scheme which resembles the limited-angle reconstruction setting.

Results are shown relevant to four temporal volumes in figure 7. SART 3.5D with BM cleaning performed in the volume domain (top row) is affected by severe artifacts attaining to skull and cerebral tissue residuals, as well as streak artifacts. In the limited-angle SART 3.5D (mid row), the overall quality of the frames is improved, however the reconstruction quality of small vessels is poor in several regions. Namely, vessels overlapped in a specific view were not separated and, more generally, had smoothed edges. Conversely, the full SART 3.5D (bottom row) displays both a better cancellation of non-angiographic tissues and sharp patterns even for the smallest vessels, which guarantees a better quality of the TICs.

4.2. TICs modelling

In this section, the shape and the number of basis functions are compared as well as the post-processing method applied.

As to the basis function shape, table 3 compares SART 3.5D with 12 rectangular and 12 triangular basis functions. Results relevant to the subsequent A/V classification are reported. As shown, SART 3.5D with triangular basis functions yields the best overall median accuracy of 0.926 (range: 0.896–0.956), whereas when rectangular basis functions are applied an overall median accuracy of 0.873 (range: 0.835 to .0893) is achieved. As a further post-processing step we fitted the TIC with the standard Gamma variate function perfusion model. The

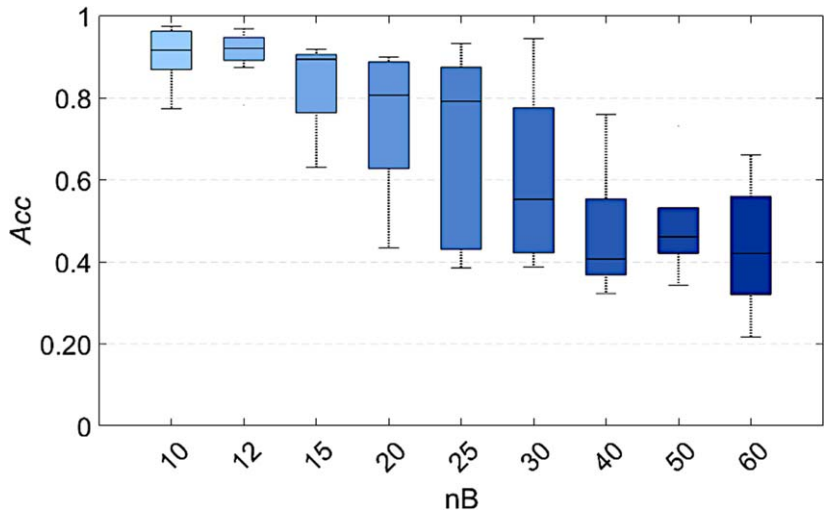

Figure 8. Boxplot of performance comparison using different number of basis function (nB). The comparison is shown in terms of accuracy (Acc) for each nB.

Table 3. Classification performance of the proposed perfusion model according to the shape of the basis function, measured as accuracy (Acc), sensitivity (Se), and specificity (Sp). Performance metrics are reported as median (interquartile range). (∗) significant by Wilcoxon rank sum.

TIC reconstruction method	Acc↑	Se↑	Sp↑
Rectangular basis functions	0.873 (0.06)	0.879 (0.02)	0.899 (0.03)
Triangular basis functions	0.926 (0.06)*	0.902 (0.04)*	0.916 (0.04)*
Triangular basis functions + Gamma fitting	0.768 (0.17)	0.740 (0.13)	0.773 (0.10)

triangular basis function combination approach demonstrated to outperform standard Gamma variate function, with a significant difference in Acc, Se, and Sp where interpolation method achieved a median Acc, Se, and Sp of 0.926, 0.902 and 0.916 versus 0.768, 0.740, 0.773.

Considering that triangular basis function outperformed all other variants a comparison of different basis functions numbers B is shown only for this shape. Acc values are compared by the box-plots of figure 8. It is noticed that the best results were at $B = 12$, with a significant difference compared to $B > 15$ (< 0.05) and with a lower IQR compared to $B < 10$.

4.3. A/V classification

First of all, the relationship between $\frac{AUC_V}{AUC}$ and vessel radius was investigated relevant to the feasibility of A/V classification based on this TIC index, as shown in figure 9, for a representative subject.

The smallest vessels in the lower 40 radius percentiles were compared to the large vessels in the 60 upper percentiles. The Gaussian fittings show a large overlap in the former case and good separation in the latter. Similar results on several randomly chosen subjects determined our choice to perform A/V classification on the set of the 60% of larger vessel, letting the smallest 40% in an unclassified 'gray-zone'.

Table 4 highlights the significant classification improvement with the subject specific $T_{A/V}$ optimization compared with a constant $T_{A/V} = T/2 = 6$ s.

Indeed, the optimal $T_{A/V}$ ranged in [4.75–6.98] s, approximately centred on $T/2$ but with large subjective differences. The Gaussian modes were located at 0.47 (0.10) and 0.72 (0.08) for the arteries and the veins, respectively. The width of Gaussians (as std) were 0.043 (0.018) and 0.02 (0.015) and the normalized weights 0.42 (0.12) and 0.58 (0.08) for the arterial and venous Gaussian, respectively. The overlap area of the two Gaussian tails was 5.8% (2.18), which confirmed that the 60% subsets showed good bimodal separation in all subjects. However, this indicates about a 6% of uncertain voxels to be added to the 'grey-zone' upon the 40% of small vessels *a priori* excluded.

In figure 10(a), the surface rendering of arteries (red) and veins (blue) classified in the set of 60% of larger vessels are shown in two representative cases. The arterial and the venous anatomical architectures are clearly displayed from left to right.

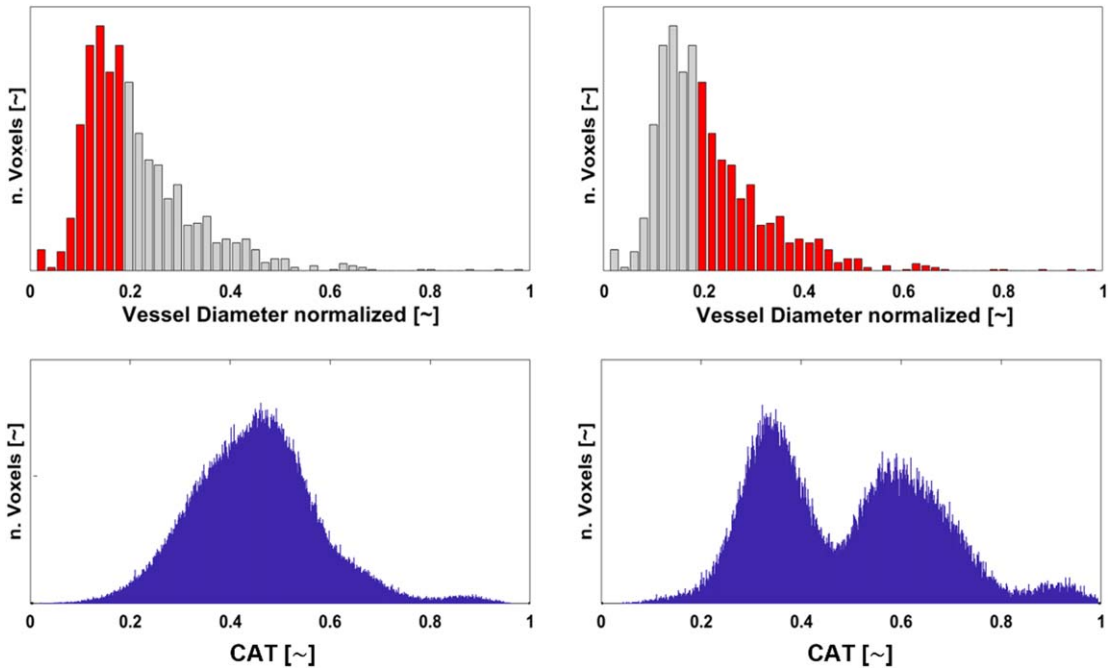

Figure 9. Comparison between CAT histogram referred to small (left) and large (righ) vessels.

Table 4. Classification performance of the proposed $T_{A/V}$ data driven computation is compared to $T_{A/V}$ computed as in Barra *et al* (2016). The metrics computed are accuracy (Acc), sensitivity (Se), and specificity (Sp). Performance metrics are reported as median (interquartile range). $*$: $p < 0.05$, Wilcoxon rank sum.

	Acc↑	Se↑	Sp↑
Constant T_{AV}	0.783 (0.09)	0.773 (0.17)	0.712 (0.13)
Adaptive T_{AV}	0.926 (0.06)*	0.902 (0.04)*	0.916 (0.04)*

In figure 10(b), relevant to the two cases, a comparison between the 60% set and the validation set is performed for the arteries (red) and veins (blue). The light red and blue vessels highlight the difference voxels in the 60% sets and not in the validation sets of arteries and veins, respectively. Interestingly, the 60% and the classification criteria after SART 3.5D are able to capture higher order arterial and venous branches compared to the validation sets, which were subject to a semiautomatic low-angle reconstruction. The opposite difference (voxels in the validation set and not in the 60% set) was virtually empty and accordingly not shown.

4.4. CAT versus Gamma based perfusion parameters

In figure 11, the CAT index (SART 3.5D, 12 triangular basis functions) is compared with indexes from gamma-curve fitting (Thompson *et al* 1964) of the 12 time samples provided by 12 rectangular basis functions. The significantly higher scores by the CAT index clearly indicate that the gamma curve, proposed to model CM dynamics after bolus injection is less suited to model the infusion protocol considered in this study.

4.5. Contrast arrival time maps and 4D DSA

In figure 12, time-resolved 3D DSA are shown according to two different criteria. The first row shows the static vascular map in four different frames. The second row shows maps of the TIC intensities $\mu(t)$ in four subsequent frames at $t = 5.5, 6.75, 9.5$, and 12 s. Lateral MIPs are shown by the hot colour scale. It is possible to appreciate the contrast change in vasculature reconstructed by the SART 3.5D TICs starting in the arterial and next contrasting the veins. The temporal volumes represented in figure 12 midline are obtained by multiplying the temporal vascular masks shown in the top row for the 3D DSA. This leads to obtaining a series of 3D DSA frames over time where each voxel is assigned an intensity value. The frames shown in the midline are intended to visually reflect the dynamics of the contrast passage. In particular, being an infusion protocol, the acquisition captures the wash in phase but not the wash out phase (this can be seen above all in figure 3, where the frames of the 2D-DSA are shown). Therefore, the flow rate of the contrast remains continuous for the duration of the

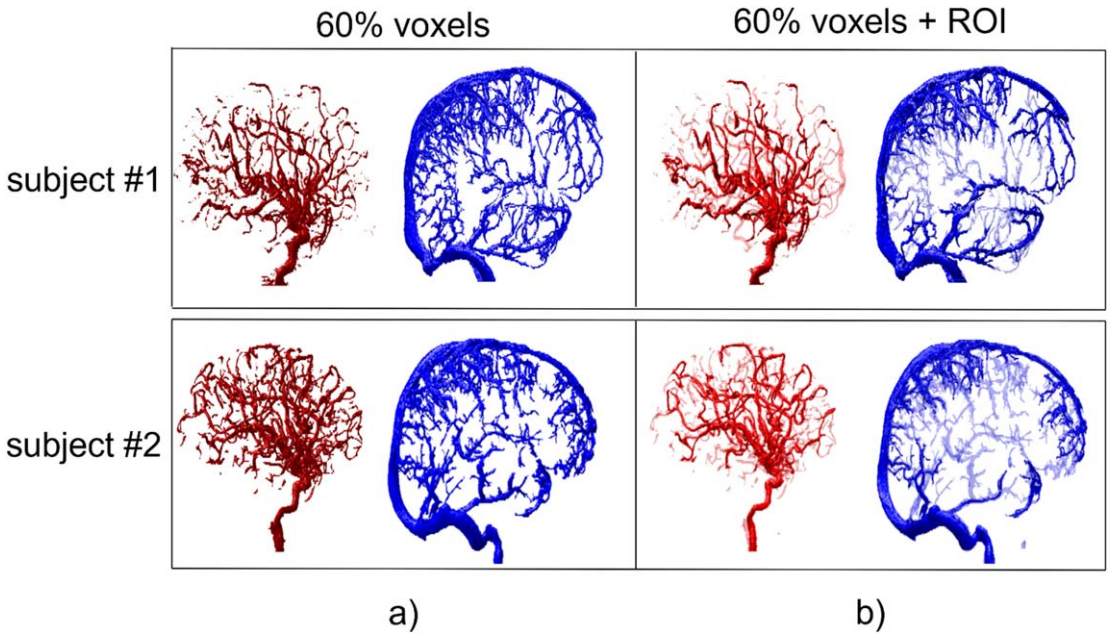

Figure 10. (a) Arterial (red) and venous (blue) compartments are represented separately and include the selected vascular voxels according to diameter and connectivity criteria (60% of angiography). (b) Arterial and venous compartments are represented in two shades. Light red and blue capture the vessels belonging to the 60% of the angiographic voxels and not included in the validation sets which are represented in dark tones.

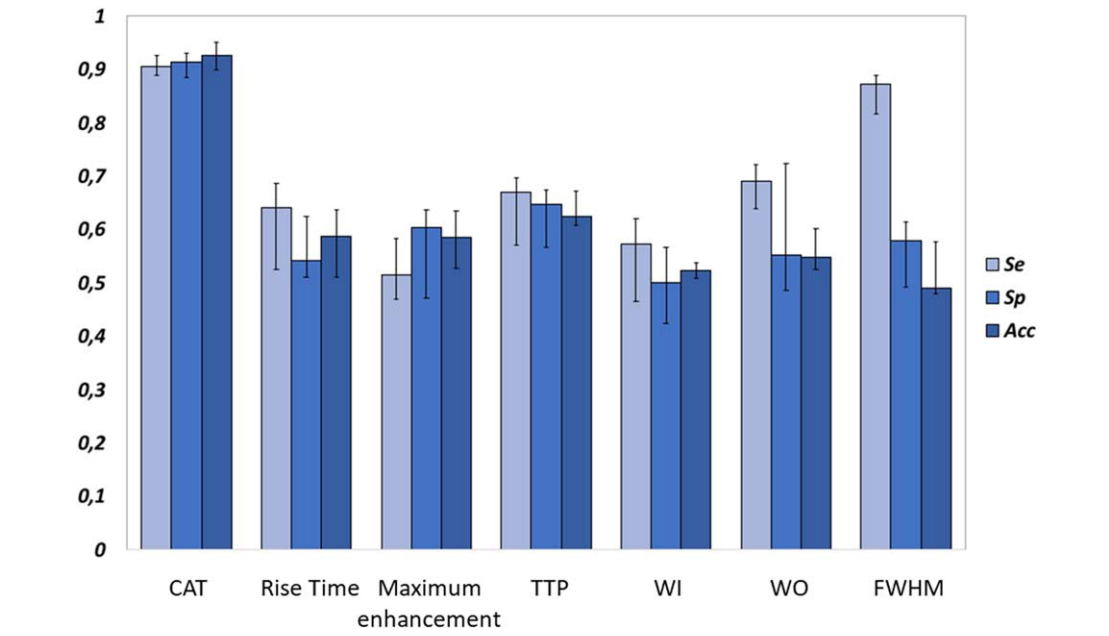

Figure 11. Bar graph showing the median values and inter-quartile range of the Se, Sp, Acc for each of the perfusion parameters computed on the selected TICs. Perfusion parameters considered are the following: rise time, maximum enhancement, time to peak (TTP), wash in (WI) and wash out (WO) rate and the full curve width at half maximum (FWHM). The bar height indicates the median value while the 'error-bar' stands for the inter-quartile range.

acquisition in the arteries, higher in the ICA. This phenomenon leads the arteries to exhibit a much higher contrast enhancement than the venous district. The full CAT map is similarly shown as lateral MIP in the bottom raw, rightmost panel. CAT values are represented by the HSV color code in the range from CAT $=$ 4.5 (red) to CAT $=$ 9.5 s (blue). To facilitate the reading of the full CAT map, progressively wider CAT ranges are shown in the previous three panels. From the left-most: (i) CAT [0, 5.5], (ii) CAT [0, 6.75], and (iii) CAT [0, 9.5]. A comparison of the corresponding frames in the top and the bottom rows clearly shows that the

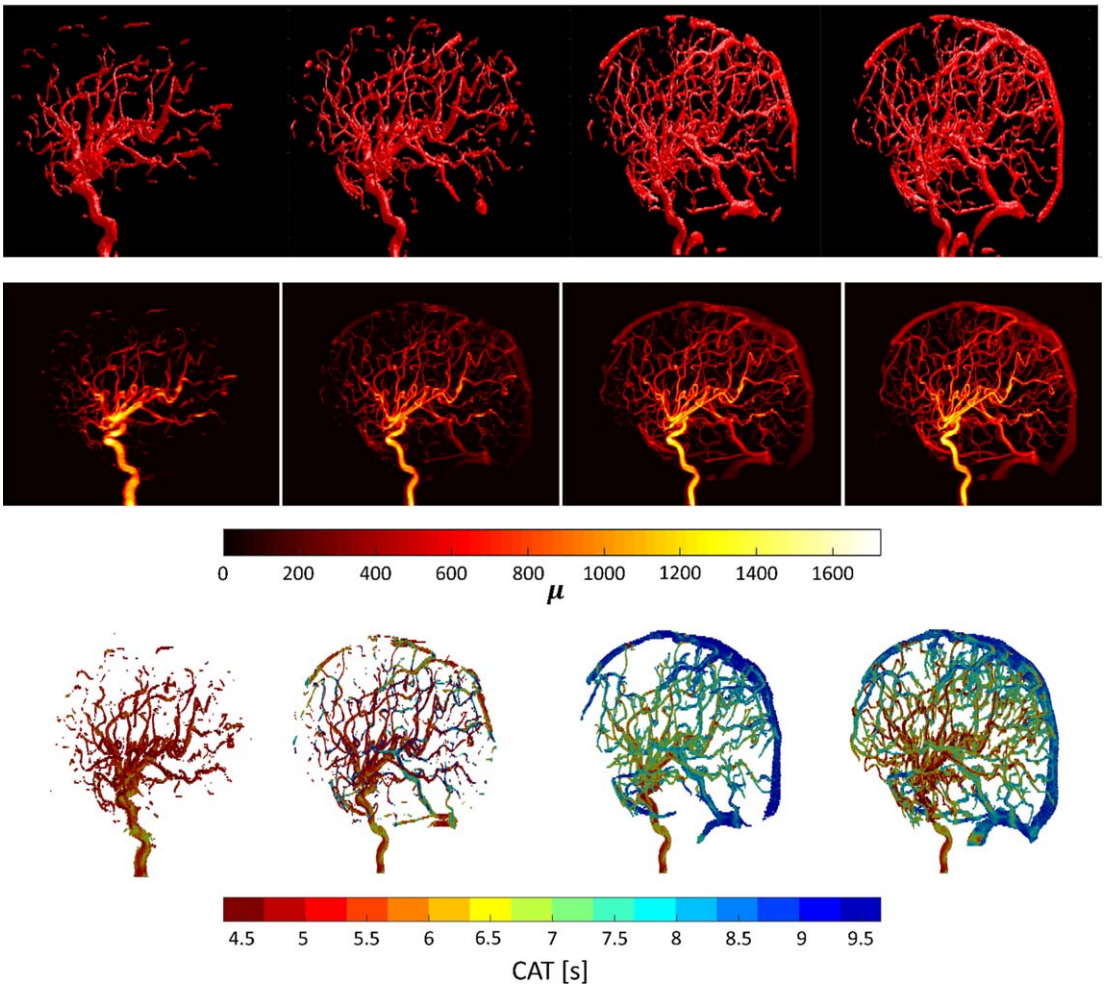

Figure 12. In the top row the 3D volume rendering. In the middle row the intensity MIP of the temporal volume, in the last the contrast arrival maps in four time frames.

CM intensity progression from arteries to veins (top) is well paralleled by the appearance of higher and higher CAT values, thus confirming this index as a valuable descriptor of the overall dynamics in single TICs.

4.6. Computational time

The automatic algorithm we propose was able to time-resolve and generate A/V classification for all considered 3D DSA cases in an average time of approximately ~5 min. The most computationally intensive step is the TIC computation. This step relies on an iterative reconstruction technique which requires $n = 4$ iterations until convergence is reached (around 52 s each iteration on a standard PC, in Matlab). While the classification step took an average time of approximately 20 s. The processing protocols were running on a Windows 10 Professional 64 bit operating system, AMD Ryzen 9 5900 × 12-Core Processor, 3.70 GHz, 128 GB RAM.

5. Discussion

This study addressed the extraction of 4D information from 3D CBCT DSA protocols (i.e. a 3.5D strategy). It started from a previous proof of concept (Barra *et al* 2016) on small and simple digital phantoms and analyzed whether a step-up to real clinical data applications was feasible. The extension to clinical datasets demanded first to address a more complex geometry with a consequent considerable computational load. it is worth mentioning the crude size issues passing to a 400-fold number of voxels with about a 400^2-fold larger system matrix, from 5 phantom vessels to the hundreds of segmented angiographic limbs. Second, image artifacts (e.g. patient motion) and hemodynamic and CM infusion variability from subject to subject had to be considered as well. Accordingly, our contributions can be summarized as follows: (i) SART was re-implemented as a dynamical and sparse variant of the classical SART; (ii) a specifically designed bone-mask (BM) subtraction in the 2D projection after 3D motion correction, ahead of the 3.5D dynamic reconstruction; (iii) attentive

validation of angiographic segmentation, which is a core prior to the targeted dynamic reconstruction; (iv) adaptive TIC analysis and A/V classification driven by subject specific statistics; (v) comparison of TIC parameterizations.

The study addressed CBCT DSA datasets, based on a 12 s BM scan and 12 s CE scan, with infusion of the CM in the ICA. Importantly, it was a fully standard protocol used in preparation to brain surgery (Cardinale *et al* 2015), i.e. no extra Rx exposure, CM dosage, and scan time was required, diversly from other methods (Matsumoto *et al* 2005, Mendrik *et al* 2010, Laue *et al* 2013, Havla *et al* 2015, Shirasaka *et al* 2017, Meijs and Manniesing 2018, 2019).

A major task was to improve the convergence regularization using subsets. Grouping updates into subsets was unavoidably limited to single angular views, i.e. SART, to save the temporal meaning of angles in the SART 3.5D dynamic context. Also, the computation of system matrix coefficients required optimization in favor of the distance-driven strategy. Comparisons with the previous ART3.5D done in the development phase are not shown in this study, since the adopted solutions are in the mainstream of the numerical algorithms' theory (Barra *et al* 2016), nonetheless, this passage represented a core turning point towards real applications.

Clinical data imposed specific pre-processing phases to compensate movements between the BM and the CE scans. This study demonstrated that best outcomes were given by the 3D alignment of the BM to the CE volume followed by BM cancellation from the raw 2D-CE projections (i.e. the 2D-DSA). This was compared to the different strategy of searching CE deviations from the BM within the 3D dynamic reconstruction, with initialization to BM and BM subtraction at the very end, in analogy with published algorithms (Chen *et al* 2008).

The mathematical demonstration presented by the previous work (Barra *et al* 2016) clearly showed the flexibility in the choice of different basis function shapes used to model the TICs with a reduced number of parameters B. However, only the simplest, non-overlapped, rectangular basis functions were tested since sufficient on simple digital phantoms. Conversely, this study presents a comparison among step-wise TICs from rectangular basis functions and linear-wise TICs from triangular basis functions. Moreover, the step-wise shape from the former ones were compared considering two post-processing algorithms: (a) spline smoothing and (b) gamma-curve fitting, which is a major model in the description of CM dynamics (Thompson *et al* 1964). Finally, SART 3.5D, which explores projection angles by a maximum orthogonality iteration strategy, was compared to a variant similar to low-angle reconstructions, thus showing the better performance of the proposed algorithm which processes the overall dynamic content of the dataset.

Barra *et al* (2016) define as A/V classification index ratio AUC_V/AUC, where AUC_V is the AUC limited to the last half of the scan [$T_{AV} = 6\ s,\ T = 12\ s$] and AUC refers to the whole scan duration. This integral strategy reveals to be robust against TICs noise and well suited to infusion protocols. Hence, it was maintained in the present study, though adapted to real cases. Notation was changed in favor of the more intuitive $CAT = T(AUC_V/AUC)$ in [s], which is useful both for A/V classification and for the dynamic mapping of angiographies. It is worth remarking that such linear rescaling has no impact on classification processes. Passing to real data required to individually set the instant $T_{A/V}$ that best separated the early phase (CM almost only in arteries) from the late one (CM reaching the veins, while persisting in the arteries, due to infusion). This individual data-driven setting revealed to be crucial in real data analysis compensating subjective differences in transport delays and random errors in the synchronization between the scan and the infusion process. This goal required to optimize the GMM clustering of CAT by setting $T_{A/V}$ at the value offering the best separation of the arterial and venous Gaussian distributions, which search was implemented by a genetic algorithm.

So, the proposed criterion, so far, is exclusively based on the CM transport delay estimated by CAT. A major focus of this study was to pinpoint potentials and limitations of this strategy, possibly opening to future studies integrating dynamic and anatomical features to further improve A/V classification. Indeed, the presented results revealed a wide CAT overlap between small arterioles and venules, impeding a clear GMM clustering. Accordingly, it was decided to compute the radius of the angiographic limbs by means of skeletonization and to address only the 60% angiographic volume of larger arterial and venous vessels, letting the rest of small vessels in a 40% 'grey-zone'. Although this choice is a clear limitation of the current A/V classification, it is in keeping with the primary goal of providing a safe and robust detection of arteries as organs at risk, which is performed only within the 60% subset, nonetheless including large to medium vessels of major surgical interest.

Detailed analyses of the relationships among limb radius, anatomical position and branching order, and the functional information provided by CAT, was beyond the scope of the present study. However, this can be a starting point to future research shedding new light over cerebrovascular transport physiology and providing effective markers of its pathological alterations.

The optimization of $T_{A/V}$ limited to the 60% angiographic volume permitted good clustering with about 6% overlap of the two Gaussian distributions. It also revealed a consistently wide range of the subjective $T_{A/V}$ over about [4.75–6.98] s, which confirmed the usefulness of the implemented subject specific approach.

The selection of a gold-standard for the A/V clustering validation deserves specific discussion. In preliminary analysis, the validation against manual labelling of arteries and veins was attempted. However, this

standard approach revealed to be unfeasible due to complexity of the angiographic structure and the consistent cohort of 60 DSAs here evaluated. In practice, manual labelling could not go beyond few vessels within the 2nd–3rd branching order, while the classification set, though limited to 60%, reached the 7th order. Hence, we had to revert to the semiautomatic procedure (Par. 3.2) based on the manual selection of low-angles best representative of the arterial and the venous phase respectively, followed by visual inspection by expert observers of the arterial and venous trees reconstructed by limited-angle (non-dynamic) SART. This approach, though acceptable for validation in the absence of other options, was not a solution to automatic A/V classification since it required manual arch selections and result verification, also given the limitations of low-angle reconstructions discussed above. Conversely, the dynamic SART 3.5D does automatically integrates all the information sparse over the 360°, alias 12 s. Indeed, the lack of a 'gold-standard' fully covering the tested set is a limitation of the presented study; however, improvements could be hardly gained within the context of sole CBCT DSA data and would require comparison with different imaging systems, in a future.

The proposed CAT index, after SART 3.5D with 12 triangular basis functions, provided the highest median accuracy (0.926) with the shortest IQR (0.056), which is a very high score, though with all the previously highlighted limitations relevant both the tested and the reference sets. Concerning SART 3.5D and TIC analysis optimization, our results showed this solution to significantly outperform alternatives relevant to rectangular basis functions, basis function number, and fixed versus adaptive $T_{A/V}$.

For the sake of completeness, we also analyzed the performance of CM dynamics indexes described in the literature. Unfortunately, to our knowledge, descriptors of bolus, first-passage protocols are described, based on gamma-curve and Gaussian fitting (Calamante 2013, Akhbardeh *et al* 2019). The latter one was not considered since obviously unfit to infusion data. Conversely, results relevant to the GMM classification performance with gamma-curve indexes were presented. A comparison with the CAT criterion showed that gamma-curve fitting is less appropriate in the description of infusion protocols. This result does by no way diminish the gamma-curve validity for bolus protocols but confirmed the utility of CAT index refinement done in this study relevant to infusion protocols.

This comparison opens a brief discussion about the preference given to infusion protocols in clinical pre-surgical and surgical contexts (Cardinale *et al* 2015). Undoubtedly, nothing better than the first passage of a bolus is suited to capture the CM dynamics. However, the primary focus of clinicians is on the 3D non-dynamic angiography, and infusion assures high contrast along most of the scan, in arteries, and a broad % of the late part of the scan, in veins. Given this strong clinical need, this study challenged the problem of extracting the dynamic features testing whether their information content was sufficient to derive the CAT index and A/V classification. Further analysis will address the flexibility of the proposed method in presence of imaging modalities which are covering less than 360° (as it might be imposed by C-arm scans) to see the boundaries of the effectiveness of the approach both in terms of contrast injection protocol and minimum coverage angle.

6. Conclusion

This study demonstrated the feasibility of automatically extracting dynamic information from clinical CBCT DSA datasets based on infusion, which is conversely conceived to optimize anatomical features of the brain angiogram in pre-surgical and surgical contexts. Through a detailed optimization of the SART 3.5D algorithm, the CM arrival time (CAT) was mapped up to vessels of the 6th—7th branching order. Accordingly, arteries and veins were labelled in a 60% of the angiographic volume, excluding a 'gray-zone' of 40% of smaller vessel, with lesser importance in surgical planning. The efficacy of design choices and settings were documented in detail by comparisons with alternatives, based on the classification of arteries and veins. A limitation was the definition of a validation 'gold-standard' extracted from the same DSA datasets via a manual definition of arterial and venous low-angle reconstruction, which requires future comparisons to 'gold-standards' provided by different imaging modalities. The algorithms applied to extract morphometric properties as the radius of vascular limbs and the SART 3.5D extracting the functional information summarized by CAT deserve future attention. Firstly, to further improve vessel classification by merging the temporal (TIC) and the morphometric (branching order and connectivity) analysis of the vascular tree. Secondly, to shed new light on the physiology of cerebrovascular transport and its pathological deviations, which impacts on vast areas, from vascular malformation to cerebrovascular degenerations close related to neurological diseases.

Acknowledgments

This research was supported by Medtronic (Boston, US) under the external research program, Grant number (ERP ID# 204). Authors would like to acknowledge Dr Patrick Helm for his technical support. We are grateful to Daniele Marinucci (Medtronic Italy) for his assistance along the setting phase of the project.

Ethical statement

Ethical approval was obtained from the Niguarda Hospital Ethical Committee on 2014, January 31.

Individual patient consent was signed for the anonymized use of preoperative imaging. The research was conducted in accordance with the principles embodied in the Declaration of Helsinki. There is not a clinical trail ID number.

Appendix

According to the iterative reconstruction methods, the image acquisition process is modeled as a linear system of equations:

$$\boldsymbol{p} = \mathbf{A} \bullet \boldsymbol{\mu}, \tag{A1}$$

where $\boldsymbol{\mu} = (\mu_j) \in \mathbb{R}^J$ depicts the unknown voxel attenuations in vector form, $\boldsymbol{p} = (p_i) \in \mathbb{R}^I$ represents the measured optical density for each projection, while $\boldsymbol{A} = (a_{ij}) \in R^{IxJ}$ is the system matrix.

ART updates $\boldsymbol{\mu}^{(n)} \rightarrow \boldsymbol{\mu}^{(n+1)}$ (i.e. from update n to update $n + 1$ of the current estimate of $\boldsymbol{\mu}$) is based on the simulated projection:

$$\bar{p}_i^n = \sum_{j=1}^{J} a_{ij}\mu_j. \tag{A2}$$

Next, the additive error $p_i - p_i^{(n)}$ is computed and the update correction is given proportionally, weighted by a_{ij}. The basic ART considers single projection ray measurement at a time and imposes a ray-by-ray updates (i.e. an iteration through the whole dataset is composed by I updates). Hence, the convergence is initially the fastest possible, but has an unstable end since no smoothing of data redundancy is included (Kak *et al* 2002). This is obtained by derived algorithms including a relaxation factor $\lambda < 1$ (percent of full correction) and grouping corrections as average of the single ones in an entire subset of data (Herman and Meyer 1993, Wang and Jiang 2004, Xu *et al* 2010).

The Simultaneous ART (SART) groups into a subset all projections from a single view angle θ, $\{p_i\}_\theta$ with index $i \in \{i\}_\theta$ (Andersen and Kak 1984). Since the introduction of SART, subset strategies have been significantly improved to optimize the tradeoff between fastness with small subsets (i.e. many updates in a single iteration) and convergence stability with large ones. A significant improvement in reconstruction smoothness was found, compared to ART (Kunz and Frangakis 2014). The SART update equation is:

$$\mu_j^{(n+1)} = \mu_j^{(n)} + \lambda \frac{1}{\sum_{i \in I_\theta} a_{ij}} \sum_{i \in I_\theta} \frac{p_i - \bar{p}_i^n}{\sum_{j=1}^{J} a_{ij}} a_{ij}. \tag{A3}$$

In this study, the relaxation factor λ was set to 0.99, a common value in the literature.

ORCID iDs

Sara El Hadji https://orcid.org/0000-0001-6479-3319
Augusto Bonilauri https://orcid.org/0000-0003-0268-3346
Elena De Momi https://orcid.org/0000-0002-8819-2734
Luca Berta https://orcid.org/0000-0003-4718-4727
Francesco Cardinale https://orcid.org/0000-0002-5141-9202
Giuseppe Baselli https://orcid.org/0000-0003-2978-1704

References

Akaike H 1974 A new look at the statistical model identification *IEEE Trans. Autom. Control* **19** 716–23

Akhbardeh A, Sagreiya H, El Kaffas A, Willmann J K and Rubin D L 2019 A multi-model framework to estimate perfusion parameters using contrast-enhanced ultrasound imaging *Med. Phys.* **46** 590–600

Akpek S, Brunner T, Benndorf G and Strother C 2005 Three-dimensional imaging and cone beam volume CT in C-arm angiography with flat panel detector *Diagn. Interventional Radiol.* **11** 10–14

Andersen A H and Kak A C 1984 Simultaneous algebraic reconstruction technique (SART): a superior implementation of the ART algorithm *Ultrason. Imaging* **6** 81–94

Barra B, De Momi E, Ferrigno G, Pero G, Cardinale F and Baselli G 2016 ART 3.5 D: an algorithm to label arteries and veins from three-dimensional angiography *J. Med. Imaging* **3** 044002

Bhattacharyya A 1943 On a measure of divergence between two statistical populations defined by their probability distributions *Bull. Calcutta Math. Soc.* **35** 99–109

Calamante F 2013 Arterial input function in perfusion MRI: a comprehensive review *Prog. Nucl. Magn. Reson. Spectrosc.* **74** 1–32
Cardinale F, Cossu M, Castana L, Casaceli G, Schiariti M P, Miserocchi A and Russo G L 2013 Stereoelectroencephalography: surgical methodology, safety, and stereotactic application accuracy in 500 procedures *Neurosurgery* **72** 353–66
Cardinale F, Pero G, Quilici L, Piano M, Colombo P, Moscato A and Cossu M 2015 Cerebral angiography for multimodal surgical planning in epilepsy surgery: description of a new three-dimensional technique and literature review *World Neurosurg.* **84** 358–67
Cardinale F, Rizzi M, d'Orio P, Casaceli G, Arnulfo G, Narizzano M and Castana L 2017 A new tool for touch-free patient registration for robot-assisted intracranial surgery: application accuracy from a phantom study and a retrospective surgical series *Neurosurg. Focus* **42** 7
Cardinale F, Rizzi M, Vignati E, Cossu M, Castana L, d'Orio P and Francione S 2019 Stereoelectroencephalography: retrospective analysis of 742 procedures in a single centre *Brain* **142** 2688–704
Chen G H and Li Y 2015 Synchronized multiartifact reduction with tomographic reconstruction (SMART-RECON): a statistical model based iterative image reconstruction method to eliminate limited-view artifacts and to mitigate the temporal-average artifacts in time-resolved CT *Med. Phys.* **42** 4698–707
Chen G H, Tang J and Leng S 2008 Prior image constrained compressed sensing (PICCS): a method to accurately reconstruct dynamic CT images from highly undersampled projection data sets *Med. Phys.* **35** 660–3
Chen K K, Guo W Y, Yang H C, Lin C J, Wu C H, Gehrisch S and Chung W Y 2017 Application of time-resolved 3D digital subtraction angiography to plan cerebral arteriovenous malformation radiosurgery *Am. J. Neuroradiol.* **38** 740–6
Christenson P C, Ovitt T W, Fisher H D, Frost M M, Nudelman S and Roehrig H 1980 Intravenous angiography using digital video subtraction: intravenous cervicocerebrovascular angiography *Am. J. Neuroradiol.* **1** 379–86
Davis B, Royalty K, Kowarschik M, Rohkohl C, Oberstar E, Aagaard-Kienitz B and Mistretta C 2013 4D digital subtraction angiography: implementation and demonstration of feasibility *Am. J. Neuroradiol.* **34** 1914–21
De Man B and Basu S 2004 Distance-driven projection and backprojection in three dimensions *Phys. Med. Biol.* **49** 2463–75
Dempster A P, Laird N M and Rubin D B 1977 Maximum likelihood from incomplete data via the EM algorithm *J. R. Stat. Soc.: Ser. B (Methodological)* **39** 1–22
Frangi A F, Niessen W J, Vincken K L and Viergever M A 1998 Multiscale vessel enhancement filtering *Int. Conf. on Medical Image Computing and Computer-Assisted Intervention* (Berlin, Heidelberg: Springer) pp 130–7
Gandhi D, Chen J, Pearl M, Huang J, Gemmete J J and Kathuria S 2012 Intracranial dural arteriovenous fistulas: classification, imaging findings, and treatment *Am. J. Neuroradiol.* **33** 1007–13
Gilard V, Proust F, Gerardin E, Lebas A, Chastan N, Fréger P and Derrey S 2016 Usefulness of multidetector-row computerized tomographic angiography for the surgical planning in stereoelectroencephalography *Diagn. Interventional Imaging* **97** 333–7
Goldberg D E 1989 *Genetic Algorithms in Search, Optimization & Machine Learning* (Reading, MA: Addison-Wesley)
Gölitz P, Struffert T, Lücking H, Rösch J, Knossalla F, Ganslandt O and Doerfler A 2013 Parametric color coding of digital subtraction angiography in the evaluation of carotid cavernous fistulas *Clin. Neuroradiol.* **23** 113–20
Gomez J, Amin A G, Gregg L and Gailloud P 2012 Classification schemes of cranial dural arteriovenous fistulas *Neurosurg. Clin.* **23** 55–62
González-Martínez J, Bulacio J, Thompson S, Gale J, Smithason S, Najm I and Bingaman W 2016 Technique, results, and complications related to robot-assisted stereoelectroencephalography *Neurosurgery* **78** 169–80
Green N E, Chen S Y J, Messenger J C, Groves B M and Carroll J D 2004 Three-dimensional vascular angiography *Curr. Probl. Cardiol.* **29** 104–42
Guan H and Gordon R 1994 A projection access order for speedy convergence of ART (algebraic reconstruction technique): a multilevel scheme for computed tomography *Phys. Med. Biol.* **39** 2005–22
Guan H and Gordon R 1996 Computed tomography using algebraic reconstruction techniques (ARTs) with different projection access schemes: a comparison study under practical situations *Phys. Med. Biol.* **41** 1727–43
Havla L, Schneider M, Thierfelder K M, Beyer S E, Ertl-Wagner B, Sommer W H and Dietrich O 2015 Validation of a method to differentiate arterial and venous vessels in CT perfusion data using linear combinations of quantitative time-density curve characteristics *Eur. Radiol.* **25** 2937–44
Herman G T and Meyer L B 1993 Algebraic reconstruction techniques can be made computationally efficient (positron emission tomography application) *IEEE Trans. Med. Imaging* **12** 600–9
Hong J S, Kao Y H, Chang F C and Lin C J 2019 Validating the automatic independent component analysis of DSA *Am. J. Neuroradiol.* **40** 540–2
Ilunga-Mbuyamba E, Avina-Cervantes J G, Lindner D, Cruz-Aceves I, Arlt F and Chalopin C 2016 Vascular structure identification in intraoperative 3D contrast-enhanced ultrasound data *Sensors* **16** 14
Jenkinson M and Smith S 2001 A global optimisation method for robust affine registration of brain images *Med. Image Anal.* **5** 143–56
Joseph P M 1982 An improved algorithm for reprojecting rays through pixel images *IEEE Trans. Med. Imaging* **1** 192–6
Kak A C, Slaney M and Wang G 2002 Principles of computerized tomographic imaging *Med. Phys.* **29** 107–107
Kaminogo M, Hayashi H, Ishimaru H, Morikawa M, Kitagawa N, Matsuo Y and Shibata S 2002 Depicting cerebral veins by three-dimensional CT angiography before surgical clipping of aneurysms *Am. J. Neuroradiol.* **23** 85–91
Kenney J F and Keeping E S 1962 *Mathematics of Statistics: Part 1* 3rd edn (Princeton: Van Nostrand)
Kong T Y and Rosenfeld A (ed) 1996 *Topological Algorithms for Digital Image Processing* (Amsterdam: Elsevier)
Krüger M T, Coenen V A, Jenkner C, Urbach H, Egger K and Reinacher P C 2018 Combination of CT angiography and MRI in surgical planning of deep brain stimulation *Neuroradiology* **60** 1151–8
Kullback S 1997 *Information Theory and Statistics* (United States: Courier Corporation)
Kunz M and Frangakis A S 2014 Super-sampling SART with ordered subsets *J. Struct. Biol.* **188** 107–15
Laue H O, Oei M T, Chen L, Kompan I N, Hahn H K, Prokop M and Manniesing R 2013 Automated artery and vein detection in 4D-CT data with an unsupervised classification algorithm of the time intensity curves *Medical Imaging 2013: Image Processing* vol 8669, pp 510–5 (SPIE)
Lee T C, Kashyap R L and Chu C N 1994 Building skeleton models via 3-D medial surface axis thinning algorithms *CVGIP, Graph. Models Image Process.* **56** 462–78
Li Y, Garrett J W, Li K, Wu Y, Johnson K, Schafer S and Chen G H 2018 Time-resolved C-arm cone beam CT angiography (TR-CBCTA) imaging from a single short-scan C-arm cone beam CT acquisition with intra-arterial contrast injection *Phys. Med. Biol.* **63** 075001
Lin M and Jackson E F 2012 Applications of imaging technology in radiation research *Radiat. Res.* **177** 387–97
Matsumoto M, Kodama N, Sakuma J, Sato S, Oinuma M, Konno Y and Shishido F 2005 3D-CT arteriography and 3D-CT venography: the separate demonstration of arterial-phase and venous-phase on 3D-CT angiography in a single procedure *Am. J. Neuroradiol.* **26** 635–41

Meijs M and Manniesing R 2018 Artery and vein segmentation of the cerebral vasculature in 4D CT using a 3D fully convolutional neural network *Medical Imaging 2018: Computer-Aided Diagnosis* vol 10575 (Int. Society for Optics and Photonics) 394–99
Meijs M, Pegge S A H, Murayama K, Boogaarts H D, Prokop M, Willems P W A and Meijer F J A 2019 Color-mapping of 4D-CTA for the detection of cranial arteriovenous shunts *Am. J. Neuroradiol.* **40** 1498–504
Mendrik A, Vonken E J, van Ginneken B, Smit E, Waaijer A, Bertolini G and Prokop M 2010 Automatic segmentation of intracranial arteries and veins in four-dimensional cerebral CT perfusion scans *Med. Phys.* **37** 2956–66
Minkin K, Gabrovski K, Penkov M, Todorov Y, Tanova R, Milenova Y and Dimova P 2017 Stereoelectroencephalography using magnetic resonance angiography for avascular trajectory planning: technical report *Neurosurgery* **81** 688–95
Mistretta C A 2011 Sub-Nyquist acquisition and constrained reconstruction in time resolved angiography *Med. Phys.* **38** 2975–85
Mullin J P, Shriver M, Alomar S, Najm I, Bulacio J, Chauvel P and Gonzalez-Martinez J 2016 Is SEEG safe? A systematic review and meta-analysis of stereo-electroencephalography–related complications *Epilepsia* **57** 386–401
Neumann J O, Campos B, Younes B, Jakobs M, Unterberg A, Kiening K and Hubert A 2019 Evaluation of three automatic brain vessel segmentation methods for stereotactical trajectory planning *Comput. Methods Programs Biomed.* **182** 105037
Nowell M, Rodionov R, Zombori G, Sparks R, Winston G, Kinghorn J and Duncan J 2015 Utility of 3D multimodality imaging in the implantation of intracranial electrodes in epilepsy *Epilepsia* **56** 403–13
Perin A, Gambatesa E, Galbiati T F, Fanizzi C, Carone G, Rui C B and DiMeco F 2021 The 'STARS-CASCADE' study: virtual reality simulation as a new training approach in vascular neurosurgery *World Neurosurg.* **154** e130–46
Prada F, Del Bene M, Mauri G, Lamperti M, Vailati D, Richetta C and DiMeco F 2018 Dynamic assessment of venous anatomy and function in neurosurgery with real-time intraoperative multimodal ultrasound *Neurosurg. Focus* **45** 9
Ramakonar H, Quirk B C, Kirk R W, Li J, Jacques A, Lind C R and McLaughlin R A 2018 Intraoperative detection of blood vessels with an imaging needle during neurosurgery in humans *Sci. Adv.* **4** eaav4992
Ruedinger K L, Schafer S, Speidel M A and Strother C M 2021 4D-DSA: development and current neurovascular applications *Am. J. Neuroradiol.* **42** 214–20
Sandoval-Garcia C, Royalty K, Yang P, Niemann D, Ahmed A, Aagaard-Kienitz B and Strother C 2016 4D DSA a new technique for arteriovenous malformation evaluation: a feasibility study *J. Neurointerventional Surg.* **8** 300–4
Scalzo F and Liebeskind D S 2016 Perfusion angiography in acute ischemic stroke *Comput. Math. Methods Med.* **2016** 14
Schwarz G 1978 Estimating the dimension of a model *Ann. Stat.* **6** 461–4
Scorza D, El Hadji S, Cortés C, Bertelsen Á, Cardinale F, Baselli G and De Momi E 2021 Surgical planning assistance in keyhole and percutaneous surgery: a systematic review *Med. Image Anal.* **67** 101820
Serafin Z, Strześniewski P, Lasek W and Beuth W 2012 Follow-up after embolization of ruptured intracranial aneurysms: a prospective comparison of two-dimensional digital subtraction angiography, three-dimensional digital subtraction angiography, and time-of-flight magnetic resonance angiography *Neuroradiology* **54** 1253–60
Shirasaka T, Hiwatashi A, Yamashita K, Kondo M, Hamasaki H, Shimomiya Y and Honda H 2017 Optimal scan timing for artery–vein separation at whole-brain CT angiography using a 320-row MDCT volume scanner *Br. J. Radiol.* **90** 20160634
Siddon R L 1985 Fast calculation of the exact radiological path for a three-dimensional CT array *Med. Phys.* **12** 252–5
Sparks R, Vakharia V, Rodionov R, Vos S B, Diehl B, Wehner T and Ourselin S 2017 Anatomy-driven multiple trajectory planning (ADMTP) of intracranial electrodes for epilepsy surgery *Int. J. Comput. Assist. Radiol. Surg.* **12** 1245–55
Strother C M, Bender F, Deuerling-Zheng Y, Royalty K, Pulfer K A, Baumgart J and Lindstrom M L 2010 Parametric color coding of digital subtraction angiography *Am. J. Neuroradiol.* **31** 919–24
Teng M M H, Chang F C, Lin C J, Chiang L, Hong J S and Kao Y H 2016 Peritherapeutic hemodynamic changes of carotid stenting evaluated with quantitative DSA in patients with carotid stenosis *Am. J. Neuroradiol.* **37** 1883–8
Thompson H K Jr, Starmer C F, Whalen R E and McIntosh H D 1964 Indicator transit time considered as a gamma variate *Circ. Res.* **14** 502–15
Tomasi S O, Umana G E, Scalia G, Rubio-Rodriguez R L, Cappai P F, Capone C and Winkler P A 2020 Importance of veins for neurosurgery as landmarks against brain shifting phenomenon: an anatomical and 3D-MPRAGE MR reconstruction of superficial cortical veins *Front. Neuroanat.* **14** 14
Torné R, García S, Sanroman L, Rodríguez-Hernández A, Reyes L, Tercero J and Enseñat J 2019 Safety and feasibility assessment of the O-Arm as an intraoperative angiography device in aneurysm surgery *World Neurosurgery* **127** e1159–65
Vakharia V N, Sparks R, Rodionov R, Vos S B, Dorfer C, Miller J and Duncan J S 2018 Computer-assisted planning for the insertion of stereoelectroencephalography electrodes for the investigation of drug-resistant focal epilepsy: an external validation study *Journal of Neurosurgery* **130** 601–10
Vakharia V N, Sparks R, Vos S B, McEvoy A W, Miserocchi A, Ourselin S and Duncan J S 2019 The effect of vascular segmentation methods on stereotactic trajectory planning for drug-resistant focal epilepsy: a retrospective cohort study *World Neurosurgery:* X **4** 100057
Wang G and Jiang M 2004 Ordered-subset simultaneous algebraic reconstruction techniques (OS-SART) *J. X-Ray Sci. Technol.* **12** 169–77
Xu F, Xu W, Jones M, Keszthelyi B, Sedat J, Agard D and Mueller K 2010 On the efficiency of iterative ordered subset reconstruction algorithms for acceleration on GPUs *Comput. Methods Programs Biomed.* **98** 261–70
Yushkevich P A, Piven J, Hazlett H C, Smith R G, Ho S, Gee J C and Gerig G 2006 User-guided 3D active contour segmentation of anatomical structures: significantly improved efficiency and reliability *Neuroimage* **31** 1116–28
Mistretta C 1980 *Real-time digital x-ray subtraction imaging* 4,204,225 (https://patents.google.com/patent/US4204225A/en)